

Stochastic Analysis of Cooperative Satellite-UAV Communications

Yu Tian¹, Gaofeng Pan¹, *Senior Member, IEEE*, Mustafa A. Kishk², *Member, IEEE*,
and Mohamed-Slim Alouini³, *Fellow, IEEE*

Abstract—This paper considers a dual-hop cooperative satellite- unmanned aerial vehicle (UAV) communication system including a satellite (S) and a group of cluster headers (CHs) which are respectively with a group of uniformly distributed UAVs. Specifically, the CHs serve as aerial decode-and-forward relays to forward the information transmitted by the S to the UAVs. Moreover, free-space optical (FSO) and radio frequency (RF) technologies are respectively adopted over S-CH and CH-UAV links to exploit the high directivity of FSO over long-distance transmission and the omnidirectional coverage ability of RF. The positions of the CHs in the three-dimensional space follow the Matérn hard-core point processes type-II, in which each CH cannot be closer to another by less than a predefined distance. Three different cases over CH-UAV links are considered during the performance modeling: interference-free, interference-dominated, and interference-and-noise. Then, the coverage performance of the S-CH link and the CH-UAV link in the aforementioned three cases is studied and the closed-form analytical expressions of the coverage probability (CP) over both two links are derived. Additionally, the asymptotic expressions for the CP over S-CH link and CH-UAV link in the interference-free case are derived. Finally, numerical results are provided to validate our proposed analytical models and thus some meaningful conclusions are achieved.

Index Terms—Coverage probability, free-space optical communication, Matérn hard-core point process, satellite communication, stochastic geometry, unmanned aerial vehicle.

I. INTRODUCTION

SATELLITE communication offers the advantages of large-scale coverage, abundant frequency resources, and flexibility of deployment, and has been widely applied in disaster monitoring and rescue, location and navigation, and long-distance information transmission [1]. So far, research

Manuscript received February 25, 2021; revised August 12, 2021 and October 4, 2021; accepted October 7, 2021. Date of publication October 26, 2021; date of current version June 10, 2022. This work was supported in part by the Office of Sponsored Research at KAUST and in part by NSF of China under Grant 62171031. The associate editor coordinating the review of this article and approving it for publication was M. Ding. (Corresponding author: Gaofeng Pan.)

Yu Tian, Mustafa A. Kishk, and Mohamed-Slim Alouini are with the Computer, Electrical and Mathematical Science and Engineering Division, King Abdullah University of Science and Technology (KAUST), Thuwal 23955-6900, Saudi Arabia (e-mail: yu.tian@kaust.edu.sa; mustafa.kishk@kaust.edu.sa; slim.alouini@kaust.edu.sa).

Gaofeng Pan is with the School of Cyberspace Science and Technology, Beijing Institute of Technology, Beijing 100081, China (e-mail: gaofeng.pan.cn@ieee.org).

Color versions of one or more figures in this article are available at <https://doi.org/10.1109/TWC.2021.3121299>.

Digital Object Identifier 10.1109/TWC.2021.3121299

on satellite-terrestrial communication systems has mainly focused on from the aspects of performance analysis [1]–[3], resource allocation [1], [4], [5], user scheduling [6], physical layer security analysis [7]–[9], and secrecy-energy efficiency analysis [10], [11].

Moreover, the virtues of unmanned aerial vehicles (UAVs), such as their small size, light weight, low cost, flexible and fast deployment, and scalability, have been widely used in many applications, including military investigation, disaster relief and rescue, law enforcement, aerial photography, agricultural monitoring, and plant protection [12]. As UAVs can freely change their locations, line-of-sight (LoS) communication links with ground users or stations can be quickly and efficiently established. Considerable attention has been paid to the resource allocation, trajectory planning, and physical layer security of UAV-ground communications [13]–[16]. However, it is hard to build up communication links between UAVs and remote control center in scenarios where ground facilities are destroyed by natural disasters, such as earthquakes and floods, or in inaccessible areas like deserts, oceans, and forests, which can result in out of control accidents or even crashes.

To tackle the aforementioned problems, a satellite can serve as an alternative to play a similar role as terrestrial facilities to set up reliable links between UAVs and the remote control center. Thus, by jointly applying the merits of both satellite and UAV communications, satellite-UAV communication systems can introduce more flexibility to the applications of UAVs, especially in harsh application scenarios, e.g., disaster response, natural resource exploration, Internet of Things (IoT) [5], and military applications in hostile and unfamiliar environments, compared to either traditional satellite communication systems or traditional UAV communication systems. Even though satellites may be solely competent in some of these use-cases, cost-efficient UAVs cooperating with satellites can provide more reliable communications and capture richer local information, especially when the LOS links are unavailable, e.g., satellite-to-terrestrial links are blocked by mountains, buildings, trees, etc.

Motivated by these observations, numerous researchers have designed and studied satellite-UAV communications in which UAVs work as aerial relays to assist communication between a satellite and terrestrial terminals [17]–[21], or between a satellite and aerial terminals [22]. In [17], the outage performance of hybrid satellite/UAV terrestrial non-orthogonal multiple access networks in which one UAV served as

a relay to forward signals to ground users was investigated, and the optimal location of the UAV to maximize the sum rate was achieved. The authors in [18] analyzed the outage probability (OP) of a hybrid satellite-terrestrial network in which a group of UAVs are mobile in a three-dimensional (3D) cylindrical space and act as relays. The ergodic capacity was evaluated in [20] for an asymmetric free-space optical (FSO)/radio frequency (RF) link in satellite-UAV-terrestrial networks while FSO communication was adopted in the satellite-UAV links. The energy-efficient beam-forming was investigated in [19] for a satellite-UAV-terrestrial system in which a multi-antenna UAV works as a relay. The authors in [22] studied beam management and self-healing in satellite-UAV mesh millimeter-Wave networks and addressed the beam misalignment issues between the UAV head and satellite/ground base station. The satellite-UAV-ground integrated networks were also used for green IoT and the authors of [21] studied how to optimize the transmit power allocation and UAV trajectory to achieve the maximum vehicle rate. Meanwhile, some researchers have worked on IoT applications of the hybrid/cognitive satellite-UAV networks in which there are no communications between the satellite and UAVs [23], [24]. In [23], IoT computing tasks can be offloaded to UAV servers or cloud servers through satellites and a learning-based approach was developed to allocate resources and schedule tasks. In [24], a satellite and a swarm of UAVs serve their own IoT devices, and a process-oriented multi-domain resource allocation algorithm was proposed to improve the efficient massive wide-area access.

Therefore, UAVs are normally used as aerial relays or cooperators of satellites to serve terrestrial terminals in most previous works on satellite-UAV communication systems. It is worthwhile to investigate the performance of satellite-UAV systems in cases where UAVs can only communicate with the satellite and function as terminals for specialized application purposes, e.g., photography, observation, surveillance, and military strikes in harsh environments. When numerous UAVs are deployed, very-high-gain antennas for RF communications or high-accuracy laser receiving systems for FSO communications cannot be equipped with UAVs due to their rigorous hardware limitations [25]. To guarantee the communication quality of the satellite-UAV link in which large path-loss leads to very weak received signals, aerial relays with advanced receiving facilities can be deployed to improve communication between the satellite and UAVs.

Furthermore, traditional satellite communication links are generally established via RF links; however, the information transmitted over such long-distance RF transmission links is quite vulnerable to being wiretapped because of its broadcasting property [1]. Due to its inherent features, including strong directivity, high security, low risk of eavesdropping, and low interference among different beams, FSO technology has been considered and developed as a promising alternative for the link between a satellite and aerial planes [2], [8].

Motivated by these aforementioned observations, in this work we consider a cooperative satellite-UAV communication system consisting of a satellite (S) and a group of common airplanes/UAVs with superior hardware resources serving as

cluster headers (CHs), each with a group of uniformly distributed UAVs. Specifically, S first transmits information to CHs via FSO links to exploit the high directivity over the long-distance transmission of FSO technology so as to safeguard the information security, then CHs respectively decode the received information and forward the recoded information to the UAVs around them using RF technology. Considering that each CH has its own serving space, the positions of CHs in 3D space follow Matérn hard-core point processes (MHCPP) type-II [26], in which each CH cannot be closer to the other CHs than a predefined distance. Moreover, the distribution of UAVs obeys a homogeneous Poisson point processes (HPPP) in the serving space of each CH.

Though considerable research has studied the performance of traditional terrestrial wireless networks in two-dimensional space using MHCPP [27]–[29], their achievements cannot be directly applied to the 3D scenario considered in this work. In [30] and [31], though the authors worked on the performance analysis of 3D MHCPP, the proposed analysis model only works for the case that the path loss exponent, namely, α_r , is greater than the dimension number of the considered space, namely, 3 for the 3D aerial space. Therefore, their results are not applicable to most of practical air-to-air communication scenarios. Especially, the analysis models presented in the two aforementioned references cannot be applied in the open free aerial space in which the communication links among UAVs are with $\alpha_r < 3$ [32]. Moreover, the authors of [33] utilized 3D binomial point process (BPP) instead of 3D MHCPP to avoid this defect existing in [30] and [31].

The main contributions of this work are summarized as follows.

1) Compared with [33], in which (a) the distribution of UAVs with fixed numbers follow 3D BPP, (b) small-scale fading is not considered, and (c) the statistical randomness of the interfering signals in 3D space was approximated by using the Gamma distribution via the central limit theorem, in this work (a) 3D MHCPP is utilized to make the system model more general, (b) Nakagami- m fading is employed to cover more network scenarios like troposphere and terrestrial spaces in which the impacts of multi-path propagation cannot be neglected, and (c) a more accurate moment generating function (MGF) of the summation of interfering signals over CH-UAV RF links is derived considering the randomness of the 3D locations of CHs.

2) Compared with [30] and [31], we address the issue that path loss exponent $\alpha_r > 3$ in 3D MHCPP by introducing the maximum interference distributed range D_{\max} . α_r can be set as small as 2 which can accurately describes the LOS aerial communications. We also adopt Nakagami- m fading model instead of Rayleigh model to make the analysis more general.

3) Compared with [30], [31], and [33], in which non-closed-form analytical expressions were presented for the performance indices while considering 3D interfering scenarios, in this work closed-form analytical expressions are respectively derived for the coverage probability (CP) over S-CH FSO links and CH-UAV RF links in interference-free, interference-dominated, and interference-and-noise cases.

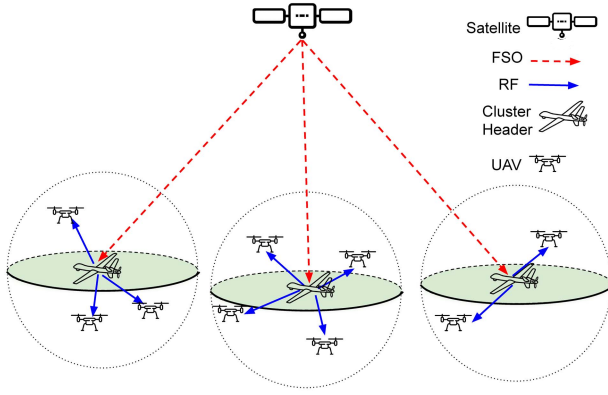


Fig. 1. System model.

4) The asymptotic expressions for the CP are derived and the diversity orders are calculated for both the S-CH FSO and CH-UAV RF links for the interference-free case.

The rest of this paper is organized as follows. In Section II, the considered dual-hop cooperative satellite-UAV communication system is described. In Sections III, IV, and V, the coverage performance of S-CH FSO links, CH-UAV RF links, and the end-to-end (e2e) coverage performance of S-CH-UAV links are investigated. In Section VI, the numerical results are presented and discussed. Finally, the concluding remarks are provided in Section VII.

II. SYSTEM MODEL

In this work, a dual-hop cooperative satellite-UAV communication system, which contains a satellite (S) and a group of cluster headers (CHs)¹ that are respectively with a group of uniformly distributed UAVs, is considered, as shown in Fig. 1. Specifically, S first delivers its intensity-modulated optical signals to CHs by using multibeam wavelength division multiplexing-FSO technology [34], and then each CH decodes its received signals by optical direct detection and forwards the recorded information to the UAVs within its serving space.^{2,3}

A. S-CH FSO Link

It is assumed that FSO communication technology is adopted over S-CH links to exploit its high directivity in order to minimize the probability that the transmitted information is wiretapped during the long-distance transmission over S-CH links.⁴ This assumption is reasonable as FSO technology

¹In practical, CHs can be common airplanes piloted by human or the UAVs with superior hardware resources, which is capable of providing data receiving, processing, and forwarding functionalities to serve as aerial relays between S and UAVs.

²This cluster-based CH-UAV network has the advantages of easy management and low operating cost, and is especially suitable for the highly dynamic scenarios with resource-constrained terminals.

³As most of the modulation schemes implemented in FSO systems are usually different from those adopted in RF communication systems, the decode-and-forward (DF) technology is applied at the CHs rather than the amplify-and-forward technology.

⁴Normally, the distance of satellite-aerial transmissions ranges from hundreds of to tens of thousands of kilometers, depending on the orbit height of the satellite.

has already been designed and implemented, and is to be tested for inter-satellite and space-to-aerial communications benefiting from its own unique advantages, e.g., Space Development Agency plans to demonstrate optical communications from satellites to a military drone aircraft in the summer of 2021 [35].

Also, to reflect and meet practical aerial scenarios, in the considered system model, the locations of the CHs in 3D space are assumed to obey an MHCPP type-II,⁵ denoted by Φ_{CH} , with an intensity of λ_{CH} and a minimum distance D_{min} between different CHs. To obtain the proposed MHCPP, a three-step thinning process is applied. Firstly, candidate points whose distribution follows an HPPP Φ_P with an intensity λ_P are generated in such a way that these points are uniformly distributed in the considered 3D space \mathcal{V} and the number of candidate points $N_P = |\Phi_P|$ has a probability mass function of Poisson distribution with a mean $\lambda_P V$ [36] expressed as

$$\Pr\{N_P = n\} = \frac{(\lambda_P V)^n}{n!} \exp(-\lambda_P V), \quad (1)$$

where V is the volume of \mathcal{V} .

Then, secondly, each candidate point is assigned to an independent mark which obeys a uniform distribution ranging from 0 to 1. Thirdly, whether each candidate point is associated with the smallest mark is individually checked and compared with all other points around it within a distance, D_{min} . If true, the point can remain in Φ_{CH} . Otherwise, the point will be eliminated. From this process, one can see that each CH exhibits a spherical repulsion space with the radius D_{min} .

Thus, according to [36, Eq. (5.56)], the relationship between λ_{CH} and λ_P is given as

$$\lambda_{CH} = \frac{1 - \exp\left(-\frac{4}{3}\pi D_{min}^3 \lambda_P\right)}{\frac{4}{3}\pi D_{min}^3}. \quad (2)$$

As shown in Fig. 2, CHs are distributed inside a 3D space \mathcal{V} that is defined by subtracting a spherical cone with radius R from another spherical cone with radius $R + H_U$. The two spherical cones share the same center O and apex angle ξ_0 . The volume of \mathcal{V} is $V = \frac{2\pi}{3}(1 - \cos\xi_0)[(R + H_U)^3 - R^3]$.

For the FSO link, the intensity modulated direct detection is utilized. According to [37, Eq. (3.1.27)], the electrical signal received by CH_k after photoelectric conversion is

$$y_k = \eta P_S G_S G_R \left(\frac{\lambda}{4\pi d_k}\right)^2 h_p h_a h_l s_k + n_k, \quad (3)$$

where P_S is the transmit optical power, η is the effective photoelectric conversion ratio, G_S and G_R are the telescope gains of the transmitter and receiver, λ is the wavelength of the laser, d_k is the distance from S to CH_k , h_p is the random attenuation caused by beam spreading and misalignment fading, h_a is the random attenuation caused by atmospheric turbulence, h_l is the atmospheric loss, s_k is the transmitted symbol with the

⁵Here, we assume that the UAVs work in clusters and each cluster has its own working space. Moreover, one can easily see that, if two clusters are too close to each other, they will merge to one cluster; otherwise, serious interference between/among two or more close UAV clusters will inevitably arise, resulting in the collapse of UAV systems.

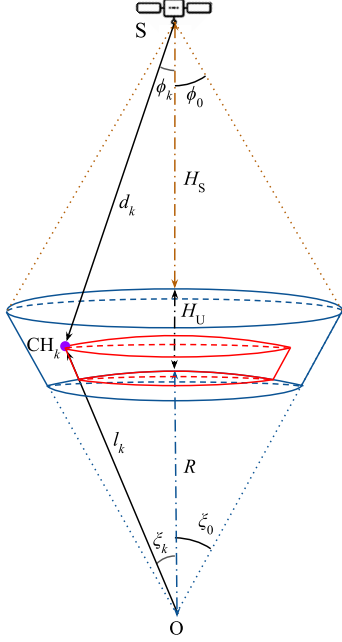


Fig. 2. S-CH system model.

average power of 1, and n_k is the additive white Gaussian noise (AWGN) of CH_k with power N_F .

In this work, we adopt the fading model mentioned in [2], which considers the atmospheric loss h_l , the atmospheric turbulence h_a with Gamma-Gamma distribution, and the misalignment fading h_p with a zero boresight pointing error model. Then, the CDF of the channel power gain $h = h_l h_a h_p$ can be given as

$$F_h(x) = \frac{\omega^2}{\Gamma(\alpha)\Gamma(\beta)} G_{2,4}^{3,1} \left(\frac{\alpha\beta}{A_0 h_l} x \middle| \begin{matrix} 1, \omega^2 + 1 \\ \omega^2, \alpha, \beta, 0 \end{matrix} \right), \quad (4)$$

where $\Gamma(\cdot)$ is the Gamma function, α and β are the effective number of small-scale and large-scale eddies of the scattering environment, $G(\cdot)$ is the Meijer- G function, A_0 is the fraction of power collected by the detector when there is no pointing error, and ω is the ratio between the equivalent beam radius and the standard deviation of pointing error displacement at the receiver.

In this context, the SNR of the signal received at CH_k is

$$\gamma_k = \frac{\eta^2 P_S^2 G_S^2 G_R^2 \lambda^4 h^2}{(4\pi)^4 d_k^4 N_F}. \quad (5)$$

Lemma 1: Given d_k , the CDF of γ_k is

$$F_{\gamma_k|d_k^2}(x) = \frac{\omega^2}{\Gamma(\alpha)\Gamma(\beta)} G_{2,4}^{3,1} \left(\Xi d_k^2 \sqrt{x} \middle| \begin{matrix} 1, \omega^2 + 1 \\ \omega^2, \alpha, \beta, 0 \end{matrix} \right), \quad (6)$$

where $\Xi = \frac{\alpha\beta(4\pi)^2 \sqrt{N_F}}{A_0 h_l \eta \lambda^2 P_S G_S G_R}$.

Proof: From (4) and (5), we can get

$$\begin{aligned} F_{\gamma_k|d_k^2}(x) &= \Pr\{\gamma_k \leq x\} \\ &= \Pr\left\{ \frac{\eta^2 P_S^2 G_S^2 G_R^2 \lambda^4 h^2}{(4\pi)^4 d_k^4 N_F} \leq x \right\} \end{aligned}$$

$$\begin{aligned} &= \Pr\left\{ h \leq \frac{(4\pi)^2 d_k^2 \sqrt{N_F} x}{\eta \lambda^2 P_S G_S G_R} \right\} \\ &= \frac{\omega^2}{\Gamma(\alpha)\Gamma(\beta)} G_{2,4}^{3,1} \left(\Xi d_k^2 \sqrt{x} \middle| \begin{matrix} 1, \omega^2 + 1 \\ \omega^2, \alpha, \beta, 0 \end{matrix} \right), \quad (7) \end{aligned}$$

where $\Xi = \frac{\alpha\beta(4\pi)^2 \sqrt{N_F}}{A_0 h_l \eta \lambda^2 P_S G_S G_R}$. \square

Proposition 1: When $D_{\min} \ll V^{\frac{1}{3}}$, CHs are approximately independently and uniformly distributed in \mathcal{V} .

Proof: Please refer to Appendix A. \square

Lemma 2: The PDF of d_k^2 is

$$f_{d_k^2}(x) = \frac{\pi}{2VL} [\tau_2^2(x) - \tau_1^2(x)], \quad (8)$$

where $\frac{d_{\min}^2}{2} \leq x \leq \frac{d_{\max}^2}{2}$, $d_{\min} = H_S$, $d_{\max} = \sqrt{R^2 + L^2 - 2RL \cos \xi_0}$, $L = H_S + H_U + R$, $\tau_2(x) = \min\{R + H_U, L \cos \xi_0 - \sqrt{x - L^2 \sin^2 \xi_0}\}$, and $\tau_1(x) = \max\{R, L - \sqrt{x}\}$.

Proof: Please refer to Appendix B. \square

Theorem 1: The CDF of γ_k is

$$\begin{aligned} F_{\gamma_k}(x) &= \frac{\pi^2 b_1 \omega^2}{2M_f V L \Gamma(\alpha)\Gamma(\beta)} \sum_{i=1}^{M_f} [\tau_2^2(b_i) - \tau_1^2(b_i)] \\ &\quad \times \sqrt{1 - t_i^2} G_{2,4}^{3,1} \left(\Xi b_i \sqrt{x} \middle| \begin{matrix} 1, \omega^2 + 1 \\ \omega^2, \alpha, \beta, 0 \end{matrix} \right), \quad (9) \end{aligned}$$

where M_f is the number of points of the Chebyshev-Gauss quadrature, $t_i = \cos \frac{2i-1}{2M_f} \pi$, $b_i = b_1 t_i + b_2$, $b_1 = \frac{d_{\max}^2 - d_{\min}^2}{2}$ and $b_2 = \frac{d_{\max}^2 + d_{\min}^2}{2}$.

Proof: Using (6), the CDF of γ_k is

$$\begin{aligned} F_{\gamma_k}(x) &= \int_{\frac{d_{\min}^2}{2}}^{\frac{d_{\max}^2}{2}} F_{\gamma_k|d_k^2}(x|y) f_{d_k^2}(y) dy \\ &= \int_{\frac{d_{\min}^2}{2}}^{\frac{d_{\max}^2}{2}} \frac{\pi \omega^2}{2VL \Gamma(\alpha)\Gamma(\beta)} [\tau_2^2(y) - \tau_1^2(y)] \\ &\quad \times G_{2,4}^{3,1} \left(\Xi x \sqrt{y} \middle| \begin{matrix} 1, \omega^2 + 1 \\ \omega^2, \alpha, \beta, 0 \end{matrix} \right) dy. \quad (10) \end{aligned}$$

By setting $b_1 = \frac{d_{\max}^2 - d_{\min}^2}{2}$, $b_2 = \frac{d_{\max}^2 + d_{\min}^2}{2}$ and $t = \frac{y-b_2}{b_1}$ and employing the M_f -point Chebyshev-Gauss quadrature in the first case, (10) can be written as

$$\begin{aligned} F_{\gamma_k}(x) &= \frac{\pi b_1 \omega^2}{2VL \Gamma(\alpha)\Gamma(\beta)} \int_{-1}^1 [\tau_2^2(b_1 t + b_2) - \tau_1^2(b_1 t + b_2)] \\ &\quad \times G_{2,4}^{3,1} \left(\Xi (b_1 t + b_2) \sqrt{x} \middle| \begin{matrix} 1, \omega^2 + 1 \\ \omega^2, \alpha, \beta, 0 \end{matrix} \right) dt \\ &= \frac{\pi^2 b_1 \omega^2}{2M_f V L \Gamma(\alpha)\Gamma(\beta)} \sum_{i=1}^{M_f} [\tau_2^2(b_i) - \tau_1^2(b_i)] \\ &\quad \times \sqrt{1 - t_i^2} G_{2,4}^{3,1} \left(\Xi b_i \sqrt{x} \middle| \begin{matrix} 1, \omega^2 + 1 \\ \omega^2, \alpha, \beta, 0 \end{matrix} \right), \quad (11) \end{aligned}$$

where $t_i = \cos \frac{2i-1}{2M_f} \pi$ and $b_i = b_1 t_i + b_2$. \square

B. CH-UAV RF Link

RF communication is employed over CH-UAV links to utilize its omnidirectional coverage ability to realize information broadcasting in the local space of each CH. Moreover, in this work, we also assume that UAVs around the k th CH, CH_k , are uniformly distributed in its serving sphere, which is centered at CH_k with radius D_k , and their positions in 3D space obey an HPPP Φ_{kU} with an intensity λ_{kU} .

In the second hop shown in Fig. 1, CH_k forwards the recoded signals with the transmit power P_k to the UAVs within its serving space, namely, the UAVs within the sphere with radius D_k centered at CH_k .⁶

To guarantee that there is no intersection between the serving spaces of any two CHs (CH_k and CH_j), $D_j + D_k < D_{\min}$ ($j \neq k$) should be satisfied. The number of UAVs around CH_k , N_{kU} , follows an HPPP with the density λ_{kU} . The PMF of N_{kU} is $\Pr\{N_{kU} = n\} = (\mu^n/n!) \exp(-\mu)$, where $\mu = \frac{4\pi D_k^3}{3} \lambda_{kU}$ is the mean measure. To make the analysis tractable, we assume that all CHs have the same serving radius and the UAVs around them have the same density, namely, $D_k = D$ and $\lambda_{kU} = \lambda_U$ ($k = 1, \dots, N_{\text{CH}}$, $N_{\text{CH}} = |\Phi_{\text{CH}}|$). Meanwhile, we assume that the communication channels from CH to UAVs suffer Nakagami- m fading.⁷

Then, the PDF and CDF of channel power gain g are shown as

$$f_g(x) = \left(\frac{m}{\Omega}\right)^m \frac{x^{m-1}}{(m-1)!} \exp\left(-\frac{m}{\Omega}x\right) \quad (12)$$

and

$$F_g(x) = 1 - \sum_{i=0}^{m-1} \left(\frac{m}{\Omega}\right)^{m_i} \frac{x^{m_i}}{m_i!} \exp\left(-\frac{m}{\Omega}x\right), \quad (13)$$

respectively, where Ω is the average received power, m is the fading parameter, and $m_i = m - i - 1$. Notably, to simplify the analysis, we only consider the scenario where m is an integer in the remainder of this paper.

The free-space path-loss from CH_k to the j th ($0 < j \leq N$) UAV marked as U_j can be given by $\rho d_{kj}^{\alpha_r}$, where ρ denotes the path loss at the distance $d = 1$ m and value of ρ depends on the carrier frequency, α_r is the path-loss exponent factor, and d_{kj} is the link distance between CH_k and U_j .

Lemma 3: The PDF of d_{kj} are respectively given as

$$f_{d_{kj}}(x) = \begin{cases} \frac{3}{D^3} x^2, & 0 \leq x \leq D; \\ 0, & \text{otherwise.} \end{cases} \quad (14)$$

⁶In this work, a single antenna is considered at each UAV to reflect the rigorous hardware constraints of practical UAV systems, as well as to make this work more concise. Moreover, the interested readers can easily expand our work to multi-antenna cases by exploiting the analysis method presented here.

⁷As suggested in Chapter 3.2.3 of [38], Nakagami- m can approximate Rician fading with the parameter K , which can be deduced by the fading parameter $m = (K + 1)^2/(2K + 1)$. In other words, Nakagami- m can represent the channel fading in the case of LoS transmission, which is the typical propagation scenario for the transmissions between CHs and UAVs. Also, when m approaches infinity, Nakagami- m can be used to describe the case with no fading.

Proof: UAVs served by CH_k can be modeled as a set of independently and identically uniformly distributed points in a sphere centered at CH_k , denoted as W_k . According to [39], d_{kj} can be calculated from W_k , the PDF of which can be presented as

$$f_{W_k} = \frac{\lambda_U}{\mu} = \frac{3}{4\pi D^3}. \quad (15)$$

Therefore, the CDF of d_{kj} can be calculated as

$$F_{d_{kj}}(x) = \int_0^x \int_0^\pi \int_0^{2\pi} \frac{3}{4\pi D^3} r^2 \sin \xi d\theta d\xi dr = \begin{cases} 0, & x < 0; \\ \frac{x^3}{D^3}, & 0 \leq x \leq D; \\ 1, & D < x. \end{cases} \quad (16)$$

Then, the PDF of d_{kj} can be obtained through $f_{d_{kj}}(x) = \frac{dF_{d_{kj}}(x)}{dx}$. \square

III. PERFORMANCE ANALYSIS OVER S-CH FSO LINKS

A. Coverage Performance

CP is defined as the ergodic probability that the received SNR of a randomly selected receiver exceeds a specific threshold. Adopting (6) and given the SNR threshold γ_{th} , the CP of CH_k is given as

$$\begin{aligned} P_{\text{cov,SCH}_k}(\gamma_{\text{th}}) &= \Pr\{\gamma_k > \gamma_{\text{th}}\} = 1 - F_{\gamma_k}(\gamma_{\text{th}}) \\ &= 1 - \frac{\pi^2 b_1 \omega^2}{2M_f V L \Gamma(\alpha) \Gamma(\beta)} \sum_{i=1}^{M_f} [\tau_2^2(b_i) - \tau_1^2(b_i)] \\ &\quad \times \underbrace{\sqrt{1 - t_i^2} G_{2,4}^{3,1} \left(\Xi b_i \sqrt{\gamma_{\text{th}}} \middle| \begin{matrix} 1, \omega^2 + 1 \\ \omega^2, \alpha, \beta, 0 \end{matrix} \right)}_{MG_0}. \end{aligned} \quad (17)$$

B. Asymptotic Coverage Performance

Theorem 2: The CP at high transmit SNR ($P_S^2/N_F \rightarrow \infty$) can be expressed as

$$\begin{aligned} P_{\text{cov,SCH}_k}^\infty(\gamma_{\text{th}}) &\approx 1 - \frac{\pi^2 b_1 \omega^2}{2M_f V L \Gamma(\alpha) \Gamma(\beta)} \sum_{i=1}^{M_f} \sqrt{1 - t_i^2} [\tau_2^2(b_i) \\ &\quad - \tau_1^2(b_i)] \left[(\Xi b_i \sqrt{\gamma_{\text{th}}}) \omega^2 \frac{\Gamma(\alpha - \omega^2) \Gamma(\beta - \omega^2)}{\omega^2} + (\Xi b_i \sqrt{\gamma_{\text{th}}})^\alpha \right. \\ &\quad \left. \times \frac{\Gamma(\omega^2 - \alpha) \Gamma(\beta - \alpha)}{\alpha \Gamma(\omega^2 + 1 - \alpha)} + (\Xi b_i \sqrt{\gamma_{\text{th}}})^\beta \frac{\Gamma(\omega^2 - \beta) \Gamma(\alpha - \beta)}{\beta \Gamma(\omega^2 + 1 - \beta)} \right]. \end{aligned} \quad (18)$$

Proof: According to [40, Eq. (9.31.2)], MG_0 in (17) can be inverted as

$$MG_0 = G_{2,4}^{3,1} \left(\frac{1}{\Xi b_i \sqrt{\gamma_{\text{th}}}} \middle| \begin{matrix} 1 - \omega^2, 1 - \alpha, 1 - \beta, 1 \\ 0, -\omega^2 \end{matrix} \right). \quad (19)$$

When $P_S^2/N_F \rightarrow \infty$, using the definition of Ξ in (7), we can get that $\frac{1}{\Xi b_i \sqrt{\gamma_{\text{th}}}} \rightarrow \infty$.

Resorting to [41, Eq.(17)], when $\frac{1}{\Xi b_i \sqrt{\gamma_{\text{th}}}} \rightarrow \infty$, MG_0 can be expanded as

$$\begin{aligned} \lim_{\frac{1}{\Xi b_i \sqrt{\gamma_{\text{th}}}} \rightarrow \infty} MG_0 &= (\Xi b_i \sqrt{\gamma_{\text{th}}})^{\omega^2} \frac{\Gamma(\alpha - \omega^2)\Gamma(\beta - \omega^2)}{\omega^2} \\ &+ (\Xi b_i \sqrt{\gamma_{\text{th}}})^{\alpha} \frac{\Gamma(\omega^2 - \alpha)\Gamma(\beta - \alpha)}{\alpha\Gamma(\omega^2 + 1 - \alpha)} \\ &+ (\Xi b_i \sqrt{\gamma_{\text{th}}})^{\beta} \frac{\Gamma(\omega^2 - \beta)\Gamma(\alpha - \beta)}{\beta\Gamma(\omega^2 + 1 - \beta)}. \end{aligned} \quad (20)$$

Substituting (20) to (17), (18) can be obtained. \square

C. Diversity Order

In this work, the diversity order of the considered system is defined as

$$\Lambda = - \lim_{\bar{\gamma} \rightarrow \infty} \frac{\log(1 - P_{\text{cov}})}{\log \bar{\gamma}}, \quad (21)$$

where $\bar{\gamma}$ is the average transmit SNR and P_{cov} is the CP.

Corollary 1: The diversity order of the S-CH FSO link is $\min\{\omega^2, \alpha, \beta\}$.

Proof: From the definition of Ξ in (7), we know that $\bar{\gamma} \rightarrow \infty$ means $\Xi \rightarrow 0$. One can see that there are three additive terms in the square brackets $[\cdot]$ in (18). When $\Xi \rightarrow 0$, it is obvious that the term with the minimum power index is dominant. Thus, using (21), the diversity order can be reached as $\min\{\omega^2, \alpha, \beta\}$. \square

IV. PERFORMANCE ANALYSIS OVER CH-UAV RF LINKS

In this section, we investigate the coverage performance of CH-UAV links in three cases: interference-free, interference-dominated, and interference-and-noise. These three cases can cover all the possibilities. When FDMA, CDMA, or TDMA is utilized, there is no interference between CHs and it belongs to the interference-free case. When all CHs share the same communication resources (time slot, frequency, code, etc.) and the number of CHs are large which make the noise power negligible, interference-dominated case should be used. When all CHs are using the same communication resources and these CHs are sparsely distributed, the interfering power is comparable with the noise power and the interference-and-noise case should be considered.

A. Interference-Free Case

We will first consider the case where there is no interference from other CHs, which also represents the scenarios that the interfering CHs are too far away the receiver or the transmit power at the interfering CH is too low to incur effective interference at the target UAV, except the scenarios mentioned above.

Supposing that CH_k has the transmit power of P_{R} , the SNR at U_j in the serving space of CH_k can be expressed as

$$\gamma_{kj} = \frac{P_{\text{R}} g_{kj}}{\rho d_{kj}^{\alpha_r} N_{\text{R}}}, \quad (22)$$

where g_{kj} is the channel power gain of the CH_k - U_j link and N_{R} is the average power of the AWGN at U_j .

Theorem 3: The CDF of γ_{kj} in the interference-free case can be calculated as

$$\begin{aligned} F_{\gamma_{kj}}(x) &= 1 - \frac{3}{\alpha_r D^3} \left(\frac{\Omega P_{\text{R}}}{m \rho N_{\text{R}} \gamma_{\text{th}}} \right)^{\frac{3}{\alpha_r}} \sum_{i=0}^{m-1} \frac{1}{m_i!} \\ &\quad \times \gamma \left(m_i + \frac{3}{\alpha_r}, \frac{m \rho N_{\text{R}} D^{\alpha_r} \gamma_{\text{th}}}{\Omega P_{\text{R}}} \right). \end{aligned} \quad (23)$$

Proof: Using (13) and (14), $F_{\gamma_{kj}}(x)$ can be expressed as

$$\begin{aligned} F_{\gamma_{kj}}(x) &= \Pr\{\gamma_{kj} < x\} = \Pr\left\{ \frac{P_{\text{R}} g_{kj}}{\rho d_{kj}^{\alpha_r} N_{\text{R}}} < x \right\} \\ &= \Pr\left\{ g_{kj} < \frac{\rho d_{kj}^{\alpha_r} N_{\text{R}}}{P_{\text{R}}} x \right\} \\ &= \int_0^D F_g \left(\frac{\rho y^{\alpha_r} N_{\text{R}}}{P_{\text{R}}} x \right) f_{d_{kj}}(y) dy \\ &= 1 - \frac{3}{D^3} \sum_{i=0}^{m-1} \frac{1}{m_i!} \left(\frac{m \rho N_{\text{R}}}{\Omega P_{\text{R}}} x \right)^{m_i} \\ &\quad \times \underbrace{\int_0^D y^{\alpha_r m_i + 2} \exp\left(-\frac{m \rho N_{\text{R}}}{\Omega P_{\text{R}}} x y^{\alpha_r}\right) dy}_{I_0}. \end{aligned} \quad (24)$$

Resorting to [40, Eq. (3.381.8)], I_0 can be given as

$$I_0 = \frac{1}{\alpha_r} \left(\frac{\Omega P_{\text{R}}}{m \rho N_{\text{R}} x} \right)^{m_i + \frac{3}{\alpha_r}} \gamma \left(m_i + \frac{3}{\alpha_r}, \frac{m \rho N_{\text{R}} D^{\alpha_r}}{\Omega P_{\text{R}}} x \right), \quad (25)$$

where $\gamma(\cdot, \cdot)$ is the lower incomplete gamma function.

Substituting (25) in (24), the CDF of γ_{kj} in the interference-free case can be obtained as (23). \square

Then, the CP in this case can be achieved as

$$\begin{aligned} P_{\text{cov},kj}(\gamma_{\text{th}}) &= 1 - F_{\gamma_{kj}}(\gamma_{\text{th}}) \\ &= \frac{3}{\alpha_r D^3} \left(\frac{\Omega P_{\text{R}}}{m \rho N_{\text{R}} \gamma_{\text{th}}} \right)^{\frac{3}{\alpha_r}} \sum_{i=0}^{m-1} \frac{1}{m_i!} \\ &\quad \times \gamma \left(m_i + \frac{3}{\alpha_r}, \frac{m \rho N_{\text{R}} D^{\alpha_r} \gamma_{\text{th}}}{\Omega P_{\text{R}}} \right). \end{aligned} \quad (26)$$

1) Asymptotic Coverage Performance: In a high SNR regime, the CDF of g in Nakagami- m fading is given as [42]

$$F_g^{\infty}(x) = \frac{m^{m-1}}{(m-1)!} \left(\frac{x}{\Omega} \right)^m. \quad (27)$$

Substituting (27) in (24), we can get the asymptotic coverage probability $P_{\text{cov},kj}^{\infty}(\gamma_{\text{th}})$ as

$$\begin{aligned} P_{\text{cov},kj}^{\infty}(\gamma_{\text{th}}) &= 1 - \int_0^D F_g^{\infty} \left(\frac{\rho N_{\text{R}} \gamma_{\text{th}} y^{\alpha_r}}{P_{\text{R}}} \right) f_{d_{kj}}(y) dy \\ &= 1 - \frac{3}{D^3} \frac{m^{m-1}}{(m-1)!} \left(\frac{\rho N_{\text{R}} \gamma_{\text{th}}}{\Omega P_{\text{R}}} \right)^m \int_0^D y^{\alpha_r m + 2} dy \\ &= 1 - \frac{3m^{m-1}}{(m-1)!} \left(\frac{\rho N_{\text{R}} \gamma_{\text{th}}}{\Omega P_{\text{R}}} \right)^m \frac{D^{\alpha_r m}}{\alpha_r m + 3}. \end{aligned} \quad (28)$$

2) Diversity Order:

Corollary 2: The diversity order of the CH-UAV links in the interference-free case is m .

Proof: Substituting (28) into (21), we can obtain the diversity order as

$$\begin{aligned} & \lim_{\frac{P_R}{N_R} \rightarrow \infty} \frac{\log \left[\frac{3m^{m-1}}{(m-1)!} \left(\frac{\rho N_R \gamma_{\text{th}}}{\Omega P_R} \right)^m \frac{D^{\alpha_r m}}{\alpha_r m + 3} \right]}{\log \left(\frac{P_R}{N_R} \right)} \\ &= \lim_{\frac{P_R}{N_R} \rightarrow \infty} \frac{\log \left[\frac{(m-1)!}{3m^{m-1}} \frac{\alpha_r m + 3}{D^{\alpha_r m}} \right] + m \log \left(\frac{\Omega}{\rho \gamma_{\text{th}}} \right) + m \log \left(\frac{P_R}{N_R} \right)}{\log \left(\frac{P_R}{N_R} \right)}. \end{aligned} \quad (29)$$

When $\frac{P_R}{N_R} \rightarrow \infty$, $\log \left[\frac{(m-1)!}{3m^{m-1}} \frac{\alpha_r m + 3}{D^{\alpha_r m}} \right]$ and $m \log \left(\frac{\Omega}{\rho \gamma_{\text{th}}} \right)$ can be negligible. Finally, one can get the diversity order as m . \square

B. Interference-Dominated Case

As the receivers of the UAVs have limited sensitivity, we consider that U_j is only disturbed by these CHs within the distance of D_{\max} (usually, $D_{\max} \gg D$ and $D_{\max} \gg D_{\min}$).

To simplify the analysis, we assume that all CHs have the same transmit power P_R and the channel power gains between interfering CHs and U_j are independent and identically distributed random variables obeying the Nakagami- m distribution with parameters m and Ω . As the interfering power is much greater than the noise power [27], the signal-to-interference ratio (SIR) is considered in this case.

The received SIR at U_j around CH_k can be presented as

$$\gamma_{kj} = \frac{\frac{P_R g_{kj}}{\rho d_{kj}^{\alpha_r}}}{\sum_{i=0}^{N_I} \frac{P_R g_{ji I_i}}{\rho d_{ji I_i}^{\alpha_r}}} = \frac{g_{kj}}{I}, \quad (30)$$

where $I = \sum_{i=0}^{N_I} \frac{g_{ji I_i}}{d_{ji I_i}^{\alpha_r}}$, N_I is the number of interfering CHs, $g_{ji I_i}$ is the channel power gain between the I_i th interfering CH and U_j , and $d_{ji I_i}$ is the distance from the I_i th CH to U_j .

1) *Coverage Performance:* The CP of the RF link in this case can be written as

$$\begin{aligned} P_{\text{cov},kj}(\gamma_{\text{th}}) &= \mathbb{E}_{I,d_{kj}} [\Pr\{\gamma_{kj} \geq \gamma_{\text{th}} | I, d_{kj}\}] \\ &= \mathbb{E}_{I,d_{kj}} [\Pr\{g_{kj} \geq \gamma_{\text{th}} I d_{kj}^{\alpha_r} | I, d_{kj}\}]. \end{aligned} \quad (31)$$

Lemma 4: $P_{\text{cov},kj}(\gamma_{\text{th}})$ can be expressed as

$$\begin{aligned} P_{\text{cov},kj}(\gamma_{\text{th}}) &= \sum_{i=0}^{m-1} \frac{1}{m_i!} \left(-\frac{m\gamma_{\text{th}}}{\Omega} \right)^{m_i} \\ &\quad \times \mathbb{E}_{d_{kj}} \left\{ d_{kj}^{\alpha_r m_i} \frac{d^{m_i} \mathbb{E}_I [e^{-sI}]}{d s^{m_i}} \right\}, \end{aligned} \quad (32)$$

where $s = m\gamma_{\text{th}} d_{kj}^{\alpha_r} / \Omega$.

Proof: According to (13) and the fact that I and d_{kj} are independent, (31) can be calculated as

$$\begin{aligned} P_{\text{cov},kj}(\gamma_{\text{th}}) &= \mathbb{E}_{I,d_{kj}} \left[\sum_{i=0}^{m-1} \left(\frac{m}{\Omega} \right)^{m_i} \frac{(\gamma_{\text{th}} I d_{kj}^{\alpha_r})^{m_i}}{m_i!} \right. \\ &\quad \left. \times \exp \left(-\frac{m\gamma_{\text{th}} I d_{kj}^{\alpha_r}}{\Omega} \right) \right] \\ &= \sum_{i=0}^{m-1} \left(\frac{m}{\Omega} \right)^{m_i} \frac{\gamma_{\text{th}}^{m_i}}{m_i!} \mathbb{E}_{I,d_{kj}} \left[(I d_{kj}^{\alpha_r})^{m_i} \right. \\ &\quad \left. \times \exp \left(-\frac{m\gamma_{\text{th}} I d_{kj}^{\alpha_r}}{\Omega} \right) \right] \\ &= \sum_{i=0}^{m-1} \left(\frac{m}{\Omega} \right)^{m_i} \frac{\gamma_{\text{th}}^{m_i}}{m_i!} \mathbb{E}_{d_{kj}} \left\{ d_{kj}^{\alpha_r m_i} \right. \\ &\quad \left. \times \underbrace{\mathbb{E}_I \left[I^{m_i} \exp \left(-\frac{m\gamma_{\text{th}} d_{kj}^{\alpha_r} I}{\Omega} \right) \right]}_{I_2} \right\}. \end{aligned} \quad (33)$$

By setting $s = \frac{m\gamma_{\text{th}} d_{kj}^{\alpha_r}}{\Omega}$, I_2 can be obtained as

$$I_2 = \mathbb{E}_I [I^{m_i} e^{-sI}]. \quad (34)$$

From the definition of the Laplace transform (LT), the LT of I can be given as $\mathcal{L}_I(s) = \int_0^\infty e^{-st} f_I(t) dt = \mathbb{E}_I [e^{-sI}]$, where $f_I(t)$ is the PDF of I .

By using the differential property of LT, I_2 can be achieved as

$$\begin{aligned} I_2 &= \int_0^\infty t^{m_i} e^{-st} f_I(t) dt = (-1)^{m_i} \frac{d^{m_i} \mathcal{L}_I(s)}{ds^{m_i}} \\ &= (-1)^{m_i} \frac{d^{m_i} \mathbb{E}_I [e^{-sI}]}{ds^{m_i}}. \end{aligned} \quad (35)$$

Combining (33) and (35), (32) can be obtained. \square

To continue calculating (32), we need to work on $\mathbb{E}_I [e^{-sI}]$ and $\frac{d^{m_i} \mathbb{E}_I [e^{-sI}]}{ds^{m_i}}$.

Lemma 5: $\mathbb{E}_I [e^{-sI}]$ in (32) can be expressed as

$$\mathbb{E}_I [e^{-sI}] = \exp[\lambda_{\text{CH}} V_1 (I_3 - 1)], \quad (36)$$

where I_3 is present as

$$\begin{aligned} I_3 &= \left(\frac{m}{\Omega s} \right)^m \frac{\pi}{2d_{kj} V_1} \left[\mathcal{F} \left(\frac{4}{\alpha_r}, d_{jI_1}^{g_1}, d_{jI_1}^{\min} \right) + 2d_{kj} \mathcal{F} \left(\frac{3}{\alpha_r}, d_{jI_1}^{g_1}, d_{jI_1}^{\min} \right) \right. \\ &\quad + (d_{kj}^2 - D_{\min}^2) \mathcal{F} \left(\frac{2}{\alpha_r}, d_{jI_1}^{g_1}, d_{jI_1}^{\min} \right) + 4d_{kj} \mathcal{F} \left(\frac{3}{\alpha_r}, d_{jI_1}^{g_2}, d_{jI_1}^1 \right) \\ &\quad - \mathcal{F} \left(\frac{4}{\alpha_r}, d_{jI_1}^{\max}, d_{jI_1}^{g_2} \right) + 2d_{kj} \mathcal{F} \left(\frac{3}{\alpha_r}, d_{jI_1}^{\max}, d_{jI_1}^{g_2} \right) \\ &\quad \left. + (D_{\max}^2 - d_{kj}^2) \mathcal{F} \left(\frac{2}{\alpha_r}, d_{jI_1}^{\max}, d_{jI_1}^{g_2} \right) \right], \end{aligned} \quad (37)$$

$d_{jI_1}^{\min} = (D_{\min} - d_{kj})^2$, $d_{jI_1}^{g_1} = (D_{\min} + d_{kj})^2$, $d_{jI_1}^{g_2} = (D_{\max} - d_{kj})^2$, $d_{jI_1}^{\max} = (D_{\max} + d_{kj})^2$, $V_1 = \frac{4\pi}{3} (D_{\max}^3 - D_{\min}^3)$, $\mathcal{F}(a, b, c) = [{}_2F_1(m, m+a; m+a+1; -\frac{m}{\Omega s} b^{\frac{\alpha_r}{2}}) b^{\frac{(m+a)\alpha_r}{2}} - {}_2F_1(m, m+a; m+a+1; -\frac{m}{\Omega s} c^{\frac{\alpha_r}{2}}) c^{\frac{(m+a)\alpha_r}{2}}] \frac{2}{(m+a)\alpha_r}$, and ${}_2F_1(\cdot, \cdot; \cdot; \cdot)$ denotes Gauss hypergeometric function.

Proof: Please refer to Appendix C \square

Lemma 6: Resorting to **Lemma 5**, $\frac{d^{m_i} \mathbb{E}_I[e^{-sI}]}{ds^{m_i}}$ in (32) can be represented as

$$\frac{d^{m_i} \mathbb{E}_I[e^{-sI}]}{ds^{m_i}} = \exp(\mathcal{A}(s, d_{kj})) \left[1 + \mathbb{1}\{m_i > 0\} \times \sum_{n=1}^{m_i} \mathcal{B}(m_i, n, \mathcal{A}(s, d_{kj})) \right], \quad (38)$$

where $\mathcal{A}(s, d_{kj}) = \lambda_{\text{CH}} V_1 (I_3 - 1)$, $\mathcal{B}(m_i, n, \mathcal{A}(s, d_{kj})) = B_{m_i, n}(\mathcal{A}^{(1)}(s, d_{kj}), \dots, \mathcal{A}^{(m_i-n+1)}(s, d_{kj}))$, $B_{m_i, n}(\cdot)$ is the Bell polynomial, and $\mathcal{A}^{(n)}(s, d_{kj})$ is the n th derivative of $\mathcal{A}(s, d_{kj})$.

Proof: When $m_i = 0$,

$$\frac{d^0}{ds^0} \exp(\mathcal{A}(s, d_{kj})) = \exp(\mathcal{A}(s, d_{kj})). \quad (39)$$

When $m_i > 0$, according to Faà di Bruno's formula, we can obtain

$$\frac{d^{m_i}}{ds^{m_i}} \exp(\mathcal{A}(s, d_{kj})) = \exp(\mathcal{A}(s, d_{kj})) \sum_{n=1}^{m_i} \mathcal{B}(m_i, n, \mathcal{A}(s, d_{kj})), \quad (40)$$

where $\mathcal{A}^{(n)}(s, d_{kj})$ is the n th derivative of $\mathcal{A}(s, d_{kj})$, $\mathcal{B}(m_i, n, \mathcal{A}(s, d_{kj})) = B_{m_i, n}(\mathcal{A}^{(1)}(s, d_{kj}), \dots, \mathcal{A}^{(m_i-n+1)}(s, d_{kj}))$, and $B_{m_i, n}(\cdot)$ is the Bell polynomial. \square

Lemma 7: $\mathcal{A}^{(n)}(s, d_{kj})$ ($n > 0$) in $\mathcal{B}(m_i, n, \mathcal{A}(s, d_{kj}))$ of (38) can be represented in (41), shown at the bottom of the next page, where

$$\mathcal{F}^{(l)}(a, b, c) = \begin{cases} \mathcal{F}(a, b, c) & \text{if } l = 0 \\ \frac{2}{(m+a)\alpha_r} \left[b^{\frac{(m+a)\alpha_r}{2}} \Delta^{(l)}(s, a, b) - c^{\frac{(m+a)\alpha_r}{2}} \Delta^{(l)}(s, a, c) \right] & \text{if } l > 0 \end{cases},$$

$$\Delta^{(l)}(s, a, b) = \sum_{q=1}^l \frac{(m+a)(m)_q}{m+a+q} \times {}_2F_1\left(m+q, m+a+q; m+a+q+1; -\frac{mb^{\frac{\alpha_r}{2}}}{\Omega s}\right) \times B_{l,q}\left(f_3^{(1)}(s, b), \dots, f_3^{(l-q+1)}(s, b)\right),$$

$(m)_q = \prod_{k=0}^{q-1} (m-k)$ is the rising Pochhammer symbol, and

$$f_3^{(q)}(s, b) = (-1)^{q+1} q! \frac{mb^{\frac{\alpha_r}{2}}}{\Omega} s^{-1-q}.$$

Proof: Please refer to Appendix D. \square

Theorem 4: The CP of the RF link in the interference-dominated case can be expressed as

$$P_{\text{cov},kj}(\gamma_{\text{th}}) \approx \frac{3\pi}{2D^2 M_r} \sum_{p=1}^{M_r} \sqrt{1-t_p^2} \sum_{i=0}^{m-1} \left(-\frac{m\gamma_{\text{th}}}{\Omega}\right)^{m_i} \times \frac{b_p^{\alpha_r m_i + 2}}{m_i!} \exp\left(\tilde{\mathcal{A}}(\gamma_{\text{th}}, b_p)\right) \left[1 + \mathbb{1}\{m_i > 0\} \times \sum_{n=1}^{m_i} \mathcal{B}(m_i, n, \tilde{\mathcal{A}}(\gamma_{\text{th}}, b_p)) \right], \quad (42)$$

where $\tilde{\mathcal{A}}(\gamma_{\text{th}}, b_p) = \mathcal{A}\left(\frac{m\gamma_{\text{th}} b_p^{\alpha_r}}{\Omega}, b_p\right)$, $t_p = \cos\left(\frac{2p-1}{2M_r} \pi\right)$, $b_p = \frac{D}{2}(t_p + 1)$, $\mathcal{A}(\cdot, \cdot)$ is defined in Lemma 6 and (37), and $\mathcal{B}(\cdot, \cdot, \mathcal{A}(\cdot, \cdot))$ is defined in Lemma 6 and (41).

Proof: Substituting (14) and (38) in (32), and then substituting $s = m\gamma_{\text{th}} d_{kj}^{\alpha_r} / \Omega$, $P_{\text{cov},kj}(\gamma_{\text{th}})$ can be expressed as

$$P_{\text{cov},kj}(\gamma_{\text{th}}) = \sum_{i=0}^{m-1} \left(-\frac{m\gamma_{\text{th}}}{\Omega}\right)^{m_i} \frac{1}{m_i!} \mathbb{E}_{d_{kj}} \left\{ d_{kj}^{\alpha_r m_i} \exp(\mathcal{A}(s, d_{kj})) \times \left[1 + \mathbb{1}\{m_i > 0\} \sum_{n=1}^{m_i} \mathcal{B}(m_i, n, \mathcal{A}(s, d_{kj})) \right] \right\} = \sum_{i=0}^{m-1} \left(-\frac{m\gamma_{\text{th}}}{\Omega}\right)^{m_i} \frac{1}{m_i!} \frac{3}{D^3} \int_0^D x^{\alpha_r m_i + 2} \exp\left(\tilde{\mathcal{A}}(\gamma_{\text{th}}, x)\right) \times \left[1 + \mathbb{1}\{m_i > 0\} \sum_{n=1}^{m_i} \mathcal{B}(m_i, n, \tilde{\mathcal{A}}(\gamma_{\text{th}}, x)) \right] dx, \quad (43)$$

where $\tilde{\mathcal{A}}(\gamma_{\text{th}}, x) = \mathcal{A}\left(\frac{m\gamma_{\text{th}} x^{\alpha_r}}{\Omega}, x\right)$.

By setting $t = \frac{2x-D}{D}$ and employing the M_r -point Chebyshev-Gauss quadrature in the first case, (43) can be written as

$$P_{\text{cov},kj}(\gamma_{\text{th}}) = \sum_{i=0}^{m-1} \left(-\frac{m\gamma_{\text{th}}}{\Omega}\right)^{m_i} \frac{1}{m_i!} \frac{3}{D^3} \frac{D}{2} \times \int_{-1}^1 \left[\frac{D}{2}(t+1)\right]^{\alpha_r m_i + 2} \exp\left(\tilde{\mathcal{A}}(\gamma_{\text{th}}, \frac{D}{2}(t+1))\right) \times \left[1 + \mathbb{1}\{m_i > 0\} \sum_{n=1}^{m_i} \mathcal{B}(m_i, n, \tilde{\mathcal{A}}(\gamma_{\text{th}}, \frac{D}{2}(t+1))) \right] dt = \sum_{i=0}^{m-1} \left(-\frac{m\gamma_{\text{th}}}{\Omega}\right)^{m_i} \frac{1}{m_i!} \frac{3}{2D^2} \frac{\pi}{M_r} \times \sum_{p=1}^{M_r} b_p^{\alpha_r m_i + 2} \exp\left(\tilde{\mathcal{A}}(\gamma_{\text{th}}, b_p)\right) \sqrt{1-t_p^2} \times \left[1 + \mathbb{1}\{m_i > 0\} \sum_{n=1}^{m_i} \mathcal{B}(m_i, n, \tilde{\mathcal{A}}(\gamma_{\text{th}}, b_p)) \right], \quad (44)$$

where $t_p = \cos\left(\frac{2p-1}{2M_r} \pi\right)$ and $b_p = \frac{D}{2}(t_p + 1)$.

After reorganizing the components in (44), (42) can be obtained. \square

Moreover, the CDF of γ_{kj} can be evaluated as

$$F_{\gamma_{kj}}(x) = 1 - P_{\text{cov},kj}(x). \quad (45)$$

C. Interference-and-Noise Case

1) *Coverage Performance:* If both interference and noise are considered, the signal-to-interference-plus-noise ratio (SINR) is

$$\gamma_{kj} = \frac{\frac{P_R g_{kj}}{\rho d_{kj}^{\alpha_r}}}{\sum_{i=0}^{N_I} \frac{P_R g_{ji}}{\rho d_{ji}^{\alpha_r}} + N_R} = \frac{\frac{g_{kj}}{d_{kj}^{\alpha_r}}}{I + \frac{\rho}{P_R} N_R}. \quad (46)$$

TABLE I
VALUES OF MAIN PARAMETERS

Parameter definition	Value
Geometric parameters in Fig. 2	$H_U = 50$ km, $H_S = 35731$ km, $R = 6376$ km, $\xi_0 = \pi/800$ rad
Intensity of CHs in Eq. (1)	$\lambda_P = 0.001$
Parameters of FSO link in Eq. (3)	$P_S = 40$ dBm, $G_S = G_R = 107.85$ dB, $\lambda = 1550$ nm, $N_F = 10^{-10}$ mW, $\eta = 0.5$, $h_l = -0.35$ dB
Parameters in FSO fading model in Eq. (4)	$A_0 = 0.5$, $\omega = 1.1$, $\alpha = 2.902$, $\beta = 2.51$
Parameters in Nakagami- m fading model in Eq. (12)	$m = 5$, $\Omega = 1$
Geometric parameters in Fig. 14	$D = 1$ km, $D_{\max} = 20$ km, $D_{\min} = 2$ km
Transmit power of CH $_k$ and noise power in Eq. (22)	$P_R = 30$ dBm, $N_R = 1.5 \times 10^{-11}$ W
Free-space path-loss exponent	$\alpha_r = 2$
Path loss at the distance of 1 m	$\rho = 38.5$ dB (Operating frequency = 2 GHz)

Theorem 5: Considering interference and noise, the CP of the RF link in this case can be expressed in (47), described shown at the bottom of the page.

Proof: To include noise, I should be replaced by $I + \frac{\rho}{P} N_R$ in (34). According to [40, Eq. 1.111], we can obtain I_2 in this case as

$$\begin{aligned} I_2 &= \mathbb{E}_I \left[\left(I + \frac{\rho}{P} N_R \right)^{m_i} \exp \left(-sI - s \frac{\rho N_R}{P} \right) \right] \\ &= \exp \left(-s \frac{\rho N_R}{P} \right) \sum_{u=0}^{m_i} \binom{m_i}{u} \left(\frac{\rho N_R}{P} \right)^{m_i-u} \\ &\quad \times \mathbb{E}_I [I^u \exp(-sI)]. \end{aligned} \quad (48)$$

Combining (14), (33), (34), (35), (38), and (48), and then employing the M_r -point Chebyshev-Gauss quadrature in the first case, the CP of the RF link in this case can be obtained as (47) given on the bottom of the page. \square

V. THE E2E COVERAGE PERFORMANCE

In the considered system, we assume that the DF relay scheme is implemented at all CHs. Then, the equivalent e2e SNR from the S to terminal UAV can be given as $\gamma_{eq}^{DF} = \min\{\gamma_k, \gamma_{kj}\}$.

Corollary 3: The e2e CP for S-CH-UAV links can be finally achieved as

$$P_{cov,e2e}(\gamma_{th}) = P_{cov,SCH_k}(\gamma_{th})P_{cov,kj}(\gamma_{th}), \quad (49)$$

where $P_{cov,SCH_k}(\gamma_{th})$ is presented as (17) and $P_{cov,kj}(\gamma_{th})$ is given as (26), (42), and (47) in interference-free case, interference-dominated case, and interference-and-noise case, respectively.

Proof: The CDF of the equivalent SNR under the DF scheme, γ_{eq}^{DF} , is given as [44]

$$F_{\gamma_{eq}^{DF}}(x) = 1 - [1 - F_{\gamma_k}(x)] [1 - F_{\gamma_{kj}}(x)]. \quad (50)$$

The CP here can be written as

$$\begin{aligned} P_{cov,e2e}(\gamma_{th}) &= 1 - F_{\gamma_{eq}^{DF}}(\gamma_{th}) \\ &= [1 - F_{\gamma_k}(\gamma_{th})] [1 - F_{\gamma_{kj}}(\gamma_{th})] \\ &= P_{cov,SCH_k}(\gamma_{th})P_{cov,kj}(\gamma_{th}). \end{aligned} \quad (51)$$

\square

Though the derived analytical expressions given in this and previous sections look a little complicated, considerable time can be saved comparing with studying the considered system directly via Monte Carlo simulations, leading to greatly improved work/study efficiency for practical applications.

VI. NUMERICAL RESULTS

In this section, numerical results are provided to assess the coverage performance of the considered satellite-UAV systems, as well as to verify the proposed analytical models. In the simulation, we run 1×10^6 trials of Monte-Carlo simulations to model the randomness of the positions of

$$\begin{aligned} \mathcal{A}^{(n)}(s, d_{kj}) &= \frac{\pi \lambda_{CH}}{2d_{kj}} \left(\frac{m}{\Omega} \right)^m \sum_{l=0}^n \binom{n}{l} (-1)^{n-l} (m)_{n-l} s^{-m-n+l} \left[\mathcal{F}^{(l)} \left(\frac{4}{\alpha_r}, d_{jI_1}^{g_1}, d_{jI_1}^{\min} \right) \right. \\ &\quad + 2d_{kj} \mathcal{F}^{(l)} \left(\frac{3}{\alpha_r}, d_{jI_1}^{g_1}, d_{jI_1}^{\min} \right) + (d_{kj}^2 - D_{\min}^2) \mathcal{F}^{(l)} \left(\frac{2}{\alpha_r}, d_{jI_1}^{g_1}, d_{jI_1}^{\min} \right) + 4d_{kj} \mathcal{F}^{(l)} \left(\frac{3}{\alpha_r}, d_{jI_1}^{g_2}, d_{jI_1}^{g_1} \right) \\ &\quad \left. - \mathcal{F}^{(l)} \left(\frac{4}{\alpha_r}, d_{jI_1}^{\max}, d_{jI_1}^{g_2} \right) + 2d_{kj} \mathcal{F}^{(l)} \left(\frac{3}{\alpha_r}, d_{jI_1}^{\max}, d_{jI_1}^{g_2} \right) + (D_{\max}^2 - d_{kj}^2) \mathcal{F}^{(l)} \left(\frac{2}{\alpha_r}, d_{jI_1}^{\max}, d_{jI_1}^{g_2} \right) \right] \end{aligned} \quad (41)$$

$$\begin{aligned} P_{cov,kj}(\gamma_{th}) &\approx \frac{3\pi}{2D^2 M_r} \sum_{p=1}^{M_r} \sqrt{1-t_p^2} \sum_{i=0}^{m-1} \left(\frac{m\gamma_{th}}{\Omega} \right)^{m_i} \frac{b_p^{\alpha_r m_i + 2}}{m_i!} \exp \left(-\frac{m\gamma_{th} b_p^{\alpha_r} \rho N_R}{\Omega P_R} + \tilde{\mathcal{A}}(\gamma_{th}, b_p) \right) \\ &\quad \times \sum_{u=0}^{m_i} \binom{m_i}{u} \left(\frac{\rho N_R}{P_R} \right)^{m_i-u} (-1)^u \left[1 + \mathbb{1}\{u > 0\} \sum_{n=1}^u \mathcal{B}(u, n, \tilde{\mathcal{A}}(\gamma_{th}, b_p)) \right] \end{aligned} \quad (47)$$

the considered CHs and UAVs. Unless otherwise explicitly specified, the main parameters adopted in this section are set in Table I, presented on the top of the next page.

A. Performance Over S-CH FSO Links

In this subsection, we will study the coverage performance over S-CH links.

In Figs. 3, 4, and 5, the CP is presented for different turbulence, H_S , and pointing errors, respectively. One can easily see that CP decreases as γ_{th} increases and coverage performance can be improved while P_S increases. The increase in CP is caused by the fact that a large γ_{th} represents a small probability of coverage events. The improvement in coverage performance can be explained by the fact that a large P_S generates a large average power for the received signals, which leads to a large received SNR.

Fig. 3(a) shows that the CP with the weak turbulence outperforms the CP with the strong turbulence when γ_{th} is less than 20 dB. On the contrary, the opposite occurs when γ_{th} is greater than 20 dB. When γ_{th} is large, Fig. 3(b) depicts that the weak turbulence leads to a large $1 - P_{cov,SCH_k}$ (small P_{cov,SCH_k}) in the small P_S region, while the inverse observation is obtained in the large P_S region. When γ_{th} is small, $1 - P_{cov,SCH_k}$ in Fig. 3(c) presents the same conclusion compared with that in Fig. 3(b).

In Figs. 4(a) and 4(b), we can observe that H_S has a negative effect on the coverage performance. In other words, the CP degrades as the orbit height of the satellite increases, which denotes that path-loss increases because a large path-loss leads to a small received SNR at the CH, which results in small CP.

Fig. 5 shows that increasing w leads to improved coverage performance. This observation can be explained by the fact that a large w denotes a small standard deviation of pointing error displacement with a fixed equivalent beam radius at the receiver, resulting in a large average received power and SNR.

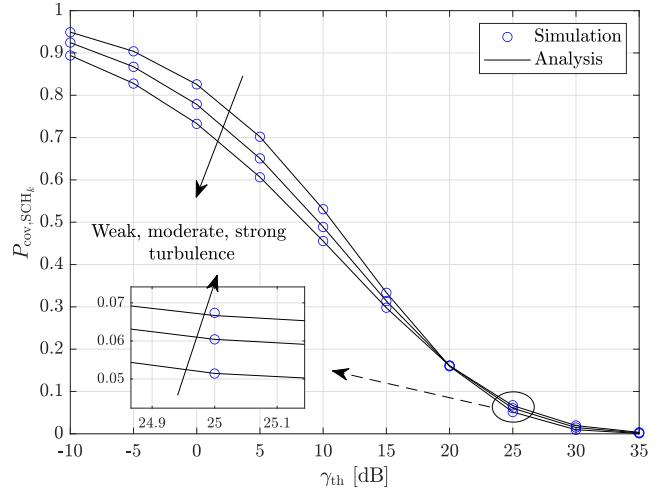
The asymptotic curves in Figs. 3(b), 3(c), and 4(b) have the same slopes in the high P_S region, as they show the same diversity order $\min\{\omega^2, \alpha, \beta\} = 1.21$. However, the three asymptotic curves in fig. 5(b) exhibit different slopes from each other because $\omega = 1.8, 1.5,$ and 1.1 result in $\min\{\omega^2, \alpha, \beta\} = 2.51, 2.25,$ and 1.21 , which cause different diversity orders.

B. Performance Over CH-UAV RF Links

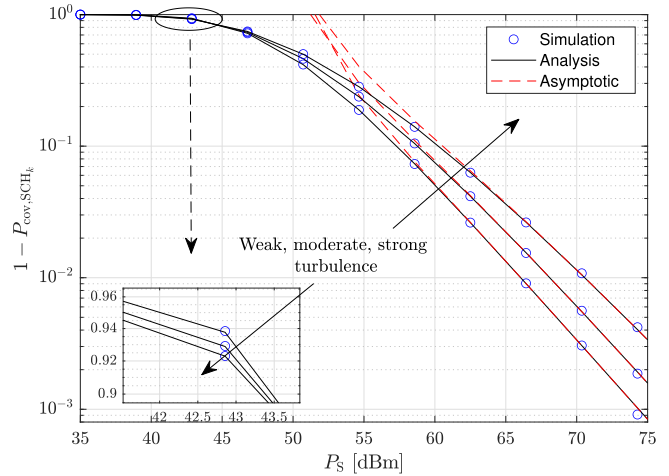
In this subsection, coverage performance for the 3 cases (interference-free, interference-dominated, and interference-and-noise) will be investigated for various main parameters.

Figs. 6 and 7 present the coverage performance for various m and D in the 3 cases. One can see that the CP with a large m outperforms the CP with a small m in small γ_{th} region. The opposite observation is achieved for large γ_{th} region. Also, it is obvious that a large D leads to a small CP, which denotes a large distributed space for the UAVs, leading to large path-loss.

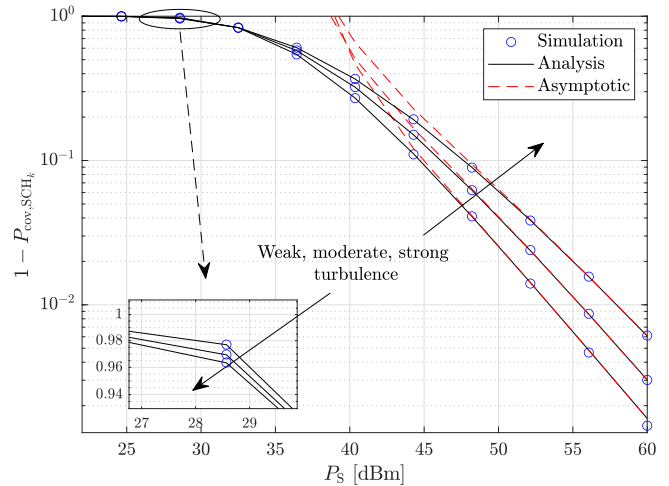
Figs. 8 and 9 investigate the influence of D_{max} and D_{min} , respectively. Clearly, D_{max} has a negative effect on the CP, while D_{min} exhibits an opposite effect in this case.



(a) P_{cov,SCH_k} versus γ_{th} with $P_S = 40$ dBm



(b) $1 - P_{cov,SCH_k}$ versus P_S with $\gamma_{th} = 30$ dB



(c) $1 - P_{cov,SCH_k}$ versus P_S with $\gamma_{th} = 5$ dB

Fig. 3. P_{cov,SCH_k} and $1 - P_{cov,SCH_k}$ over S-CH links for various kinds of turbulence (weak turbulence: $\alpha = 2.902, \beta = 2.51$; moderate turbulence: $\alpha = 2.296, \beta = 1.822$; strong turbulence: $\alpha = 2.064, \beta = 1.342$ [43]).

Also, a large D_{max} or a small D_{min} leads to more interfering CHs in the considered space, resulting in degradation of

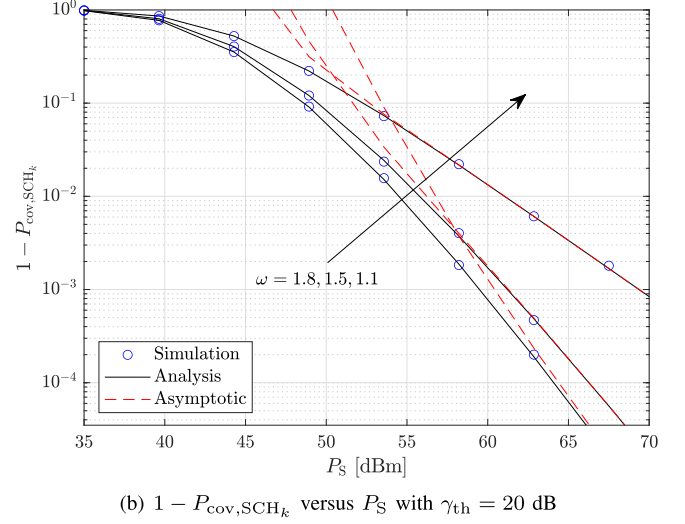
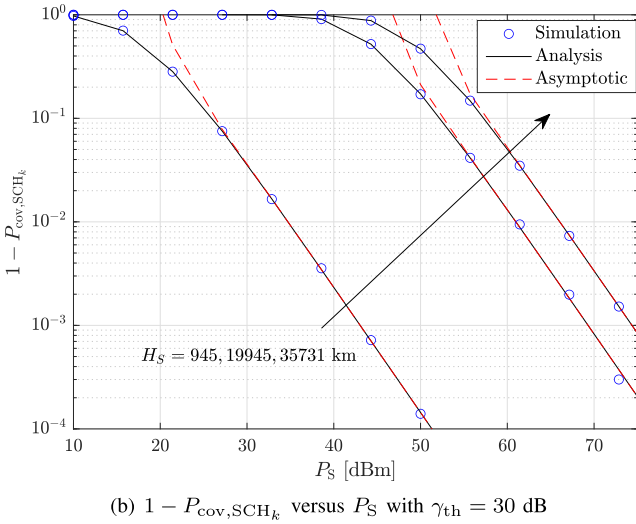
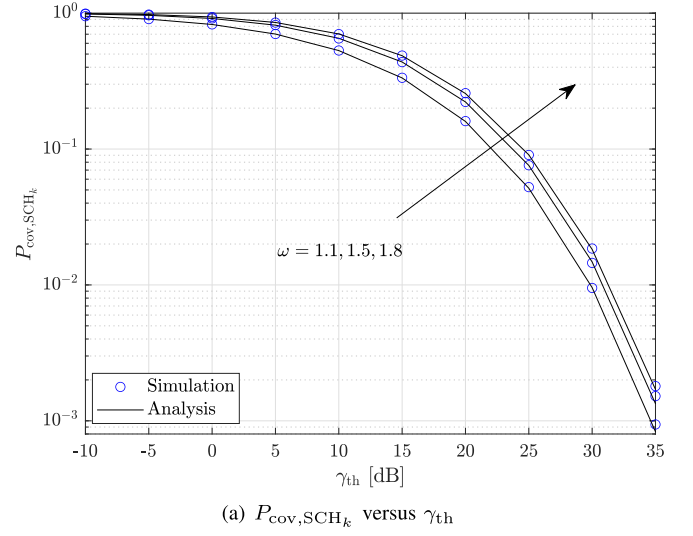
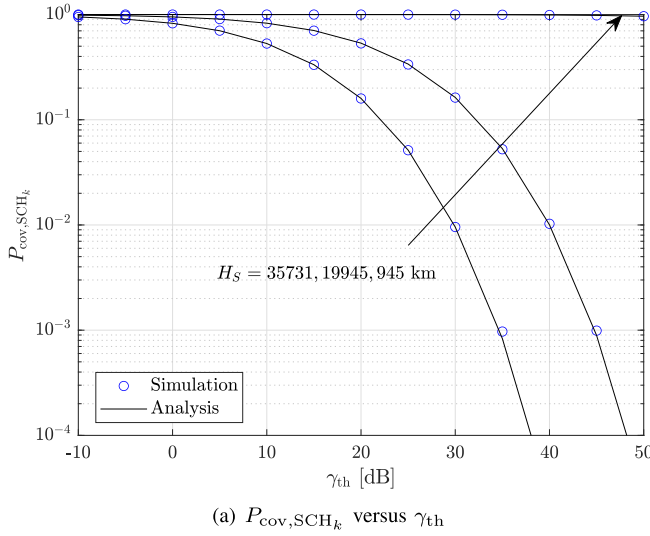


Fig. 4. $P_{\text{cov,SCH}_k}$ and $1 - P_{\text{cov,SCH}_k}$ over S-CH links for various H_S .

Fig. 5. $P_{\text{cov,SCH}_k}$ and $1 - P_{\text{cov,SCH}_k}$ over S-CH FSO links for various pointing errors.

coverage performance. It can also be observed from these two figures that the interference-and-noise analysis curves with a small $D_{\text{max}} = 3$ km and large $D_{\text{min}} = 15$ km are very close to the interference-free curve. This is caused by the fact that a small D_{max} or a large D_{min} will shrink the distributed space and then reduce the number of interfering CHs. When $D_{\text{max}} \approx D_{\text{min}}$, the amount of interfering CHs is negligible and the complex analysis model in the interference-and-noise case (47) can be approximated to the simple model in the interference-free case (26).

Fig. 10 depicts the CP versus γ_{th} for different $P_{\text{R}}/N_{\text{R}}$. It is obvious that, for interference-free and interference-and-noise cases, a larger transmitting SNR $P_{\text{R}}/N_{\text{R}}$ will bring better coverage performance. The analysis curve of interference-and-noise case is very close to that of interference-free case when $P_{\text{R}}/N_{\text{R}} = 97$ dB and the curve of interference-dominated case when $P_{\text{R}}/N_{\text{R}} = 120$ dB. When

$P_{\text{R}}/N_{\text{R}}$ is very small, $\gamma_{k,j} = \frac{g_{k,j}}{I + \frac{P_{\text{R}}}{N_{\text{R}}}} \approx \frac{P_{\text{R}} g_{k,j}}{\rho d_{k,j}^{\alpha} N_{\text{R}}}$. Therefore, the analysis model of the interference-and-noise case (47)

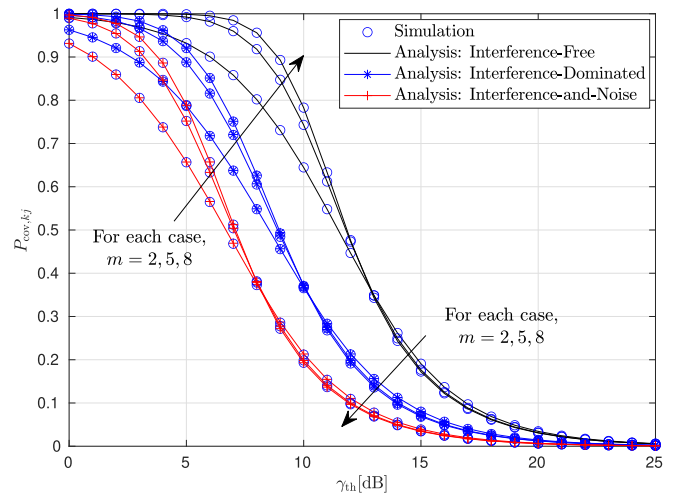


Fig. 6. $P_{\text{cov},kj}$ versus γ_{th} over CH-UAV links for different m in 3 cases.

can be approximated to the model of the interference-free case (26). Meanwhile, when $P_{\text{R}}/N_{\text{R}}$ is very large,

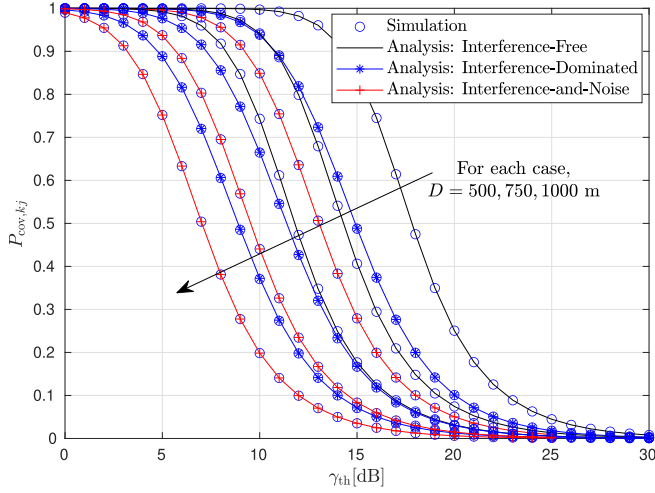


Fig. 7. $P_{cov,kj}$ versus γ_{th} over CH-UAV links for different D in 3 cases.

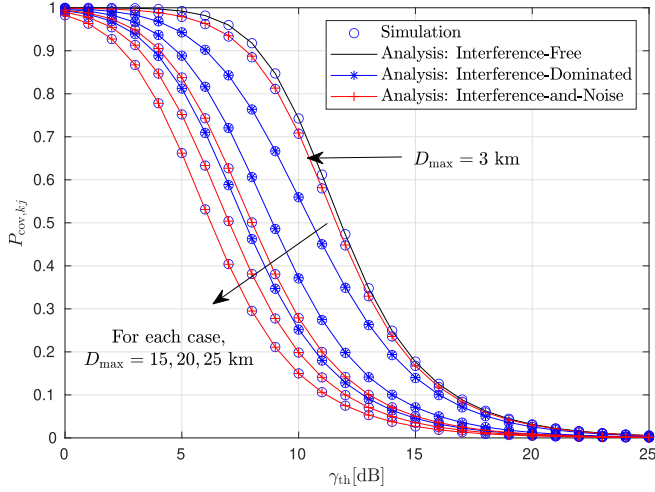


Fig. 8. $P_{cov,kj}$ versus γ_{th} over CH-UAV links for different D_{max} in the 3 cases.

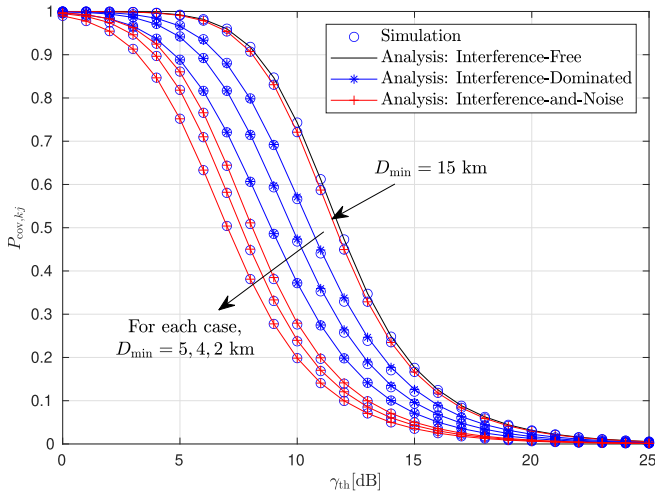


Fig. 9. $P_{cov,kj}$ versus γ_{th} over CH-UAV links for different D_{min} in the 3 cases.

$\gamma_{kj} = \frac{\frac{g_{kj}}{d_{kj}^{\alpha_r}}}{1 + \frac{P}{P_R} N_R} \approx \frac{g_{kj}}{P d_{kj}^{\alpha_r}}$ and (47) can be approximated to the model of the interference-dominated case (42).

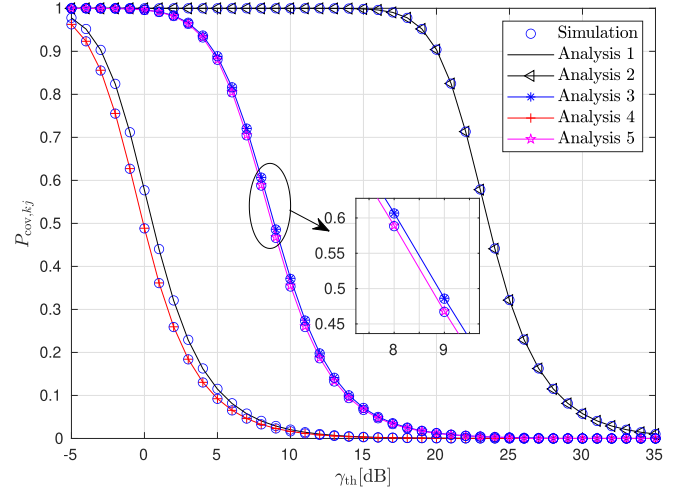


Fig. 10. $P_{cov,kj}$ versus γ_{th} over CH-UAV links for various P_R/N_R (Analysis 1 and 2 are interference-free with $P_R/N_R = 97$ dB and 120 dB; Analysis 3 is interference-dominated; Analysis 4 and 5 are interference-and-noise with $P_R/N_R = 97$ dB and 120 dB).

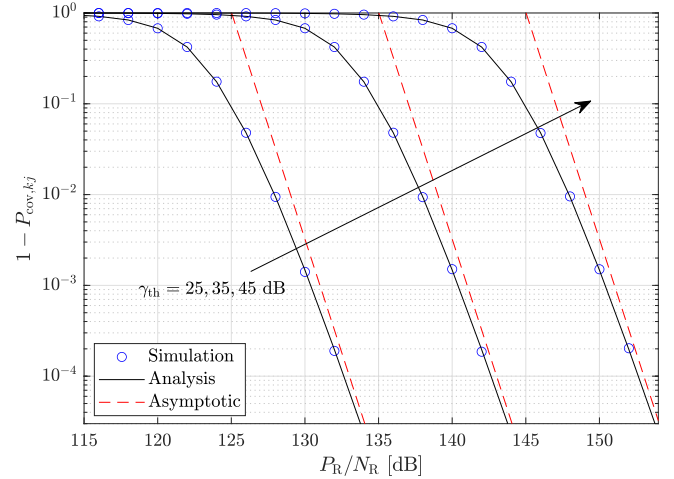


Fig. 11. $1 - P_{cov,kj}$ versus P_R/N_R over CH-UAV links for different γ_{th} in the interference-free case.

Fig. 11 shows the $1 - P_{cov,kj}$ versus P_R/N_R for various γ_{th} in the interference-free case. It is easy to see that $1 - P_{cov,kj}$ decreases or $P_{cov,kj}$ increases when P_R/N_R increases or γ_{th} decreases. These findings can be explained by the reasons proposed in the second paragraph of Section VI-A. We can also see that the three asymptotic curves have the same slope in large P_R/N_R region because they share the same diversity order m .

Furthermore, one can clearly see from Figs. 3-11 that the simulation results agree very well with the results of the analysis, and the asymptotic curves converge to the simulation and analysis curves in the high P_S region, which verifies the accuracy of our proposed analytical and asymptotic models. The slopes of asymptotic curves shows the correctness of the derived diversity order. The agreement between simulation and analysis curves for interference-dominated and interference-and-noise cases in Figs. 6-10 indicates the rationality of the approximation shown in Fig. 14.

C. The e2e Coverage Performance

From (49), we know the e2e CP is the multiplication of S-CH-link CP and CH-UAV-link CP. The findings from Figs. 3-11 are also applicable to the e2e coverage performance over S-CH-UAV links.

VII. CONCLUSION

In this paper, we studied the coverage performance of a cooperative satellite-UAV communication system with a DF relay scheme, while considering the randomness of the positions of the CHs and UAVs. Closed-form and approximated expressions for the CP over S-CH FSO links were derived. Moreover, the coverage performance over CH-UAV RF links was analyzed under three cases: interference-free, interference-dominated, and interference-and-noise. The analytical expressions for the CP under these three cases were presented, as well as the asymptotic one under the interference-free case. Finally, we show the closed-form analytical expression for the e2e CP over S-CH-UAV links.

Some useful conclusions can be drawn from the numerical results, as follows:

1) The intensity of turbulence negatively influences the CP over the S-CH FSO link in the small γ_{th} or large P_S regions, while the opposite observation is found in the large γ_{th} or small P_S regions.

2) The altitude of the satellite and pointing error negatively influence the CP over S-CH FSO links.

3) The Nakagami- m fading parameter, m , has a positive effect on the CP over CH-UAV RF links in the small γ_{th} region and a negative effect in the large γ_{th} region.

4) Over CH-UAV RF links, the coverage range D and sensitivity radius D_{max} of the CP negatively influence the CP, while the hard-core radius D_{min} has a positive effect on the CP.

5) The diversity orders over S-CH FSO links and CH-UAV links in the interference-free case are $\min\{\omega^2, \alpha, \beta\}$ and m , respectively.

6) When $D_{min} \approx D_{max}$ or P_R/N_R is very small, the analysis model of the interference-and-noise case (47) can be approximated to the model of the interference-free case (26).

7) When P_R/N_R is very large, the analysis model of the interference-and-noise case (47) can be approximated to the model of the interference-dominated case (42).

APPENDIX A: PROOF OF PROPOSITION 1

As it is difficult to prove Proposition 1 mathematically, we use Monte-Carlo simulation instead. Figs. 12 and 13 present the simulation and analysis results of the CDFs of l_k and d_k^2 with HPPP and MHCPP corresponding to different D_{min} in (2). The analysis curves are according to (52) ($y = \xi_0$) and (61) in Appendix B. The values of the other parameters adopted in this simulation are listed in Table I and $V^{\frac{1}{3}} = 46.3$ km.

The MHCPP with a specific D_{min} is thinned from the HPPP by the rule introduced in Section II. From the two figures, one can see that they present three same rules: 1. the simulation curve of the MHCPP gets close to that of the HPPP when

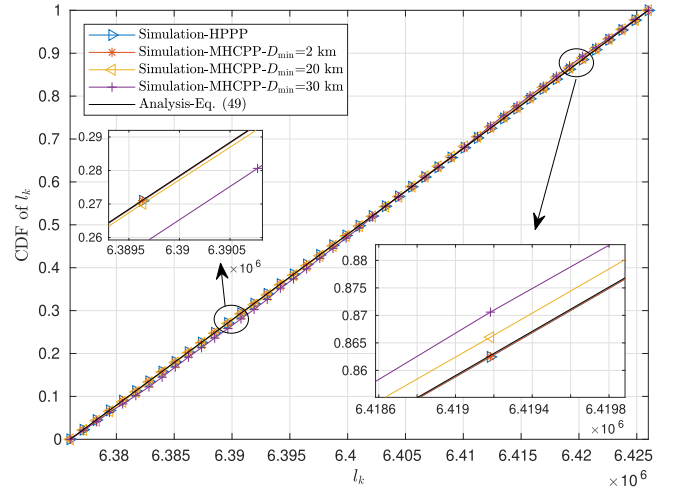


Fig. 12. CDF of l_k .

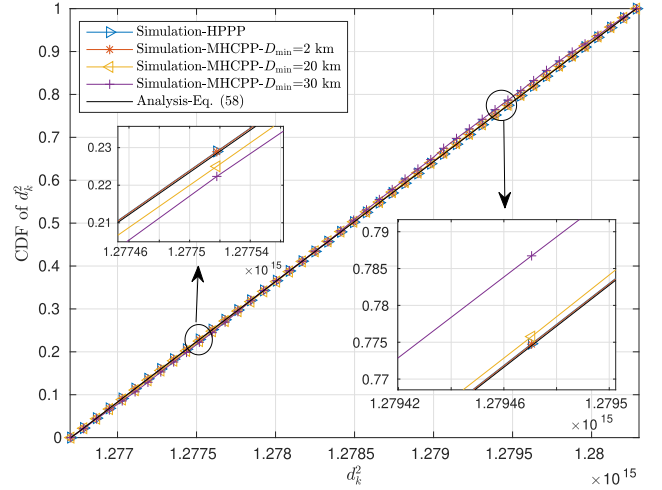


Fig. 13. CDF of d_k^2 .

D_{min} decreases; 2. the CDF curve of the MHCPP with $D_{min} = 2$ km is identical to that of the HPPP; 3. the simulation curve matches the analysis curve very well.

These three observations verify the correctness of Proposition 1, (52) ($y = \xi_0$) and (61).

APPENDIX B: PROOF OF LEMMA 2

As CHs can be regarded as a set of independently and uniformly distributed points in \mathcal{V} according to **Proposition 1**, the joint CDF of l_k and ξ_k is the ratio between the volumes of the two objects with red edges and blue edges in Fig. 2 which can be expressed as

$$F_{l_k, \xi_k}(x, y) = \frac{\int_0^{2\pi} \int_0^y \int_0^x \sin \xi d\xi \int_0^r r^2 dr}{V} = \frac{2\pi(1 - \cos y)(x^3 - R^3)}{3V}. \quad (52)$$

Then, the joint PDF of l_k and ξ_k can be written as

$$f_{l_k, \xi_k}(x, y) = \frac{\partial^2 F_{l_k, \xi_k}(x, y)}{\partial x \partial y} = \frac{2\pi x^2 \sin y}{V}. \quad (53)$$

From Fig. 2, the relationships between l_k , ξ_k , and d_k^2 can be represented as

$$d_k^2 = l_k^2 + L^2 - 2l_k L \cos \xi_k, \quad (54)$$

where $L = H_S + H_U + R$.

It can be easily seen that

$$d_{\min} \leq d_k \leq d_{\max}, \quad (55)$$

where $d_{\min} = H_S$ and $d_{\max} = \sqrt{R^2 + L^2 - 2RL \cos \xi_0}$.

To obtain the PDF of d_k^2 , we first derive the joint PDF of d_k^2 and l_k .

According to the multivariate change of variables formula, the Jacobian determinant of matrix $\partial(d_k^2, l_k)/\partial(l_k, \xi_k)$ is

$$\left| \frac{\partial(d_k^2, l_k)}{\partial(l_k, \xi_k)} \right| = \begin{vmatrix} 2l_k - 2L \cos \xi_k & 2l_k L \sin \xi_k \\ 1 & 0 \end{vmatrix} = 2l_k L \sin \xi_k. \quad (56)$$

Then, the joint PDF of d_k^2 and l_k can be achieved as

$$f_{d_k^2, l_k}(x, y) = \frac{f_{l_k, \xi_k}(x, y)}{\left| \frac{\partial(d_k^2, l_k)}{\partial(l_k, \xi_k)} \right|} = \frac{\pi y}{VL}, \quad (57)$$

where $R \leq y \leq R + H_U$ and $\cos \xi_0 \leq \cos \xi_k = \frac{y^2 + L^2 - x}{2Ly} \leq 1$.

The PDF of d_k^2 can be acquired through the integration of (57) according to l_k as follows

$$f_{d_k^2}(x) = \int_{\tau_1(x)}^{\tau_2(x)} f_{d_k, l_k}(x, y) dy = \frac{\pi}{2VL} [\tau_2^2(x) - \tau_1^2(x)]. \quad (58)$$

Observing $R \leq y \leq R + H_U$ and $\cos \xi_0 \leq \cos \xi_k = \frac{y^2 + L^2 - x}{2Ly} \leq 1$, τ_1 and τ_2 can be obtained as

$$\tau_1(x) = \max \{R, L - \sqrt{x}\} \quad (59)$$

and

$$\tau_2(x) = \min \left\{ R + H_U, L \cos \xi_0 - \sqrt{x - L^2 \sin^2 \xi_0} \right\}, \quad (60)$$

respectively.

Furthermore, the CDF of d_k^2 can be achieved as

$$F_{d_k^2}(y) = \int_{d_{\min}^2}^y f_{d_k^2}(x) dx, \quad d_{\min}^2 \leq y \leq d_{\max}^2. \quad (61)$$

APPENDIX C: PROOF OF LEMMA 5

As shown in Fig. 14, the inner blue sphere is the serving space of CH_k . The red and blue spaces are interference-free as their radii are smaller than or equal to D_{\min} to CH_k . These CHs including CH_{I_1} , which cause the interference to the typical UAV U_j , are located in the green space. d_{kj} , d_{jI_1} , and d_{kI} represent the distances between CH_k and U_j , U_j and CH_{I_1} , and U_k and CH_{I_1} , respectively.

To make the following derivation tractable, we make an approximation that CH_{I_1} is distributed in the sphere with a red dashed outline instead of the green sphere. This approximation is reasonable, as these two spheres mostly overlap and the shift between them is less than D .

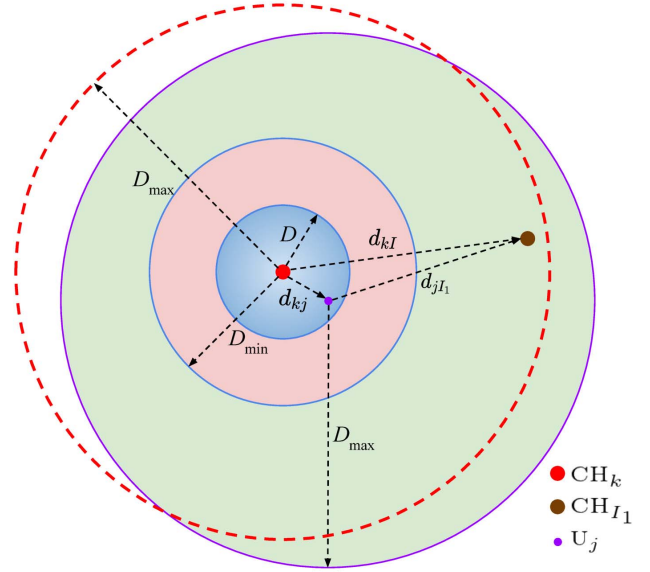


Fig. 14. CH-UAV link model.

Similar to Lemma 2, we can obtain the PDF of $d_{jI_1}^2$ given d_{kj} as

$$f_{d_{jI_1}^2 | d_{kj}}(x) = \frac{\pi [\tau_4^2(x, d_{kj}) - \tau_3^2(x, d_{kj})]}{2d_{kj} V_1}, \quad (62)$$

where $V_1 = \frac{4\pi}{3}(D_{\max}^3 - D_{\min}^3)$, $\tau_4(x, d_{kj}) = \min\{D_{\max}, \sqrt{x} + d_{kj}\}$, $\tau_3(x, d_{kj}) = \max\{D_{\min}, \sqrt{x} - d_{kj}\}$, and $d_{jI_1}^{\min} = (D_{\min} - d_{kj})^2 \leq x \leq (D_{\max} + d_{kj})^2 = d_{jI_1}^{\max}$.

It is easy to obtain that V_1 is the volume of the green space. The number of interfering CHs in this space has the probability $\Pr\{X = N_I\} = \frac{(\lambda_{\text{CH}} V_1)^{N_I}}{N_I!} e^{-\lambda_{\text{CH}} V_1}$, ($N_I = 0, \dots, \infty$).

From the definition of s in (32), we know $s > 0$. Therefore, $\mathbb{E}_I[e^{-sI}]$ can be calculated as

$$\begin{aligned} \mathbb{E}_I[e^{-sI}] &= \mathbb{E}_{N_I} \left\{ \mathbb{E}_I \left[\exp \left(-s \sum_{i=1}^{N_I} g_{jI_i} d_{jI_i}^{-\alpha_r} \right) \right] \right\} \\ &\stackrel{(a)}{=} \mathbb{E}_{N_I} \left\{ \prod_{i=1}^{N_I} \mathbb{E}_{g_{jI_i}, d_{jI_i}} \left[\exp \left(-s g_{jI_i} d_{jI_i}^{-\alpha_r} \right) \right] \right\} \\ &\stackrel{(b)}{=} \sum_{N_I=0}^{\infty} \frac{(\lambda_{\text{CH}} V_1)^{N_I}}{N_I!} \exp(-\lambda_{\text{CH}} V_1) \\ &\quad \times \left\{ \mathbb{E}_{g_{jI_1}, d_{jI_1}} \left[\exp \left(-s g_{jI_1} d_{jI_1}^{-\alpha_r} \right) \right] \right\}^{N_I} \\ &\stackrel{(c)}{=} \sum_{N_I=0}^{\infty} \frac{(\lambda_{\text{CH}} V_1 I_3)^{N_I}}{N_I!} \exp(-\lambda_{\text{CH}} V_1) \\ &\stackrel{(d)}{=} \exp(-\lambda_{\text{CH}} V_1 + \lambda_{\text{CH}} V_1 I_3), \end{aligned} \quad (63)$$

where $I_3 = \int_{d_{jI_1}^{\min}}^{d_{jI_1}^{\max}} \mathbb{E}_{g_{jI_1}} \left[\exp \left(-s g_{jI_1} x^{-\frac{\alpha_r}{2}} \right) \right] f_{d_{jI_1}^2 | d_{kj}}(x) dx$,

(a) is based on the fact that g_{jI_i} and d_{jI_i} are both independent and identically distributed random variables, (b) is obtained by substituting the PMF of N_I , (c) is achieved by substituting (62), and (d) is deduced by using the Taylor series of $\exp(-\lambda_{\text{CH}} V_1)$.

Using the MGF of the Nakagami- m function [45], $\mathbb{E}_{g_{jI_1}} [\exp(-sg_{jI_1}x^{-\frac{\alpha_r}{2}})]$ can be obtained as

$$\mathbb{E}_{g_{jI_1}} \left[\exp \left(-sg_{jI_1}x^{-\frac{\alpha_r}{2}} \right) \right] = \left(\frac{\frac{m}{\Omega_s}x^{\frac{\alpha_r}{2}}}{\frac{m}{\Omega_s}x^{\frac{\alpha_r}{2}} + 1} \right)^m. \quad (64)$$

Substituting (62) and (64) in I_3 , we deduce

$$I_3 = \left(\frac{m}{\Omega_s} \right)^m \frac{\pi}{2d_{kj}V_1} \int_{d_{jI_1}^{\min}}^{d_{jI_1}^{\max}} \frac{x^{\frac{m\alpha_r}{2}}}{\left(\frac{m}{\Omega_s}x^{\frac{\alpha_r}{2}} + 1 \right)^m} \times [\tau_4^2(x, d_{kj}) - \tau_3^2(x, d_{kj})] dy. \quad (65)$$

In the following, we will use τ_3 and τ_4 to represent $\tau_3(x, d_{kj})$ and $\tau_4(x, d_{kj})$, respectively, for convenience and discuss the integral interval in (65) in four cases according to the values of τ_3 and τ_4 .

Case 1: When $\tau_4 = D_{\max}$ which means $D_{\max} < \sqrt{x} + d_{kj}$ and $\tau_3 = D_{\min}$ which means $\sqrt{x} - d_{kj} < D_{\min}$, we can get $(D_{\max} - d_{kj})^2 < x < (D_{\min} + d_{kj})^2$. However, as $D_{\max} \gg D_{\min}$, $D_{\max} \gg D > d_{kj}$, and $D_{\max} - D_{\min} \gg 2d_{kj}$, this case does not exist.

Case 2: When $\tau_4 = \sqrt{x} + d_{kj}$ which indicates $\sqrt{x} + d_{kj} < D_{\max}$ and $\tau_3 = D_{\min}$ which indicates $\sqrt{x} - d_{kj} < D_{\min}$, we can have $(D_{\min} - d_{kj})^2 < x < (D_{\min} + d_{kj})^2$ and $\tau_4^2 - \tau_3^2 = x + 2d_{kj}\sqrt{x} + d_{kj}^2 - D_{\min}^2$ can be obtained.

Case 3: When $\tau_4 = \sqrt{x} + d_{kj}$ which denotes $\sqrt{x} + d_{kj} < D_{\max}$ and $\tau_3 = \sqrt{x} - d_{kj}$ which denotes $D_{\min} < \sqrt{x} - d_{kj}$, we deduce $d_{jI_1}^{\mathcal{G}_1} = (D_{\min} + d_{kj})^2 < x < (D_{\max} - d_{kj})^2 = d_{jI_1}^{\mathcal{G}_2}$ and $\tau_4^2 - \tau_3^2 = 4d_{kj}\sqrt{x}$.

Case 4: When $\tau_4 = D_{\max}$ which shows $D_{\max} < \sqrt{x} + d_{kj}$ and $\tau_3 = \sqrt{x} - d_{kj}$ which shows $D_{\min} < \sqrt{x} - d_{kj}$, we can obtain $(D_{\max} - d_{kj})^2 < x < (D_{\max} + d_{kj})^2$ and $\tau_4^2 - \tau_3^2 = -x + 2d_{kj}\sqrt{x} + D_{\max}^2 - d_{kj}^2$.

By using [40, Eq. 3.194.1], I_3 can be represented in (66), demonstrated shown at the bottom of the page,

where

$$\begin{aligned} \mathcal{F}(a, b, c) &= [{}_2F_1 \left(m, m+a; m+a+1; -\frac{m}{\Omega_s}b^{\frac{\alpha_r}{2}} \right) b^{\frac{(m+a)\alpha_r}{2}} \\ &\quad - {}_2F_1 \left(m, m+a; m+a+1; -\frac{m}{\Omega_s}c^{\frac{\alpha_r}{2}} \right) c^{\frac{(m+a)\alpha_r}{2}}] \\ &\quad \times \frac{2}{(m+a)\alpha_r} \end{aligned}$$

and ${}_2F_1(\cdot, \cdot; \cdot; \cdot)$ denotes the Gauss hypergeometric function.

Finally, (36) can be obtained by substituting (66) in (63).

APPENDIX D: PROOF OF LEMMA 7

According to the Leibnitz formula, $\mathcal{A}^{(n)}(s, d_{kj})$ ($n > 0$) can be expressed as

$$\mathcal{A}^{(n)}(s, d_{kj}) = \frac{\pi\lambda_{\text{CH}}}{2d_{kj}} \left(\frac{m}{\Omega} \right)^m \sum_{l=0}^n \binom{n}{l} f_1^{(n-l)}(s) f_2^{(l)}(s, d_{kj}), \quad (67)$$

where $f_1(s) = s^{-m}$ and $f_2(s, d_{kj})$ is represented in (68), presented shown at the bottom of the page.

It is easy to get the $(n-l)$ th derivative of $f_1(s)$ as

$$f_1^{(n-l)}(s) = (-1)^{n-l} (m)_{n-l} s^{-m-n+l}, \quad (69)$$

where $(m)_{n-l} = \prod_{k=0}^{n-l-1} (m-k)$ is the rising Pochhammer symbol.

To get the l th derivative of $f_2(s, d_{kj})$, we should calculate the l th derivative of $\mathcal{F}(a, b, c)$. From the definition of $\mathcal{F}(a, b, c)$ in **Lemma 5**, we first need to derive $\Delta(s, a, b) = {}_2F_1 \left(m, m+a; m+a+1; -\frac{m}{\Omega_s}b^{\frac{\alpha_r}{2}} \right)$.

When $l = 0$, $\Delta^{(0)}(s, a, b) = \Delta(s, a, b)$ can be acquired.

$$\begin{aligned} I_3 &= \left(\frac{m}{\Omega_s} \right)^m \frac{\pi}{2d_{kj}V_1} \left\{ \int_{d_{jI_1}^{\mathcal{G}_1}}^{d_{jI_1}^{\mathcal{G}_1}} \left[x^{\frac{m\alpha_r}{2}+1} + 2d_{kj}x^{\frac{m\alpha_r}{2}+1} + (d_{kj}^2 - D_{\min}^2)x^{\frac{m\alpha_r}{2}} \right] \frac{1}{\left(\frac{m}{\Omega_s}x^{\frac{\alpha_r}{2}} + 1 \right)^m} dx \right. \\ &\quad \left. + 4d_{kj} \int_{d_{jI_1}^{\mathcal{G}_1}}^{d_{jI_1}^{\mathcal{G}_2}} \frac{x^{\frac{m\alpha_r}{2}+1}}{\left(\frac{m}{\Omega_s}x^{\frac{\alpha_r}{2}} + 1 \right)^m} dx + \int_{d_{jI_1}^{\mathcal{G}_2}}^{d_{jI_1}^{\max}} \frac{-x^{\frac{m\alpha_r}{2}+1} + 2d_{kj}x^{\frac{m\alpha_r}{2}+1} + (D_{\max}^2 - d_{kj}^2)x^{\frac{m\alpha_r}{2}}}{\left(\frac{m}{\Omega_s}x^{\frac{\alpha_r}{2}} + 1 \right)^m} dx \right\} \\ &= \left(\frac{m}{\Omega_s} \right)^m \frac{\pi}{2d_{kj}V_1} \left\{ \mathcal{F} \left(\frac{4}{\alpha_r}, d_{jI_1}^{\mathcal{G}_1}, d_{jI_1}^{\min} \right) + 2d_{kj} \mathcal{F} \left(\frac{3}{\alpha_r}, d_{jI_1}^{\mathcal{G}_1}, d_{jI_1}^{\min} \right) + (d_{kj}^2 - D_{\min}^2) \mathcal{F} \left(\frac{2}{\alpha_r}, d_{jI_1}^{\mathcal{G}_1}, d_{jI_1}^{\min} \right) + 4d_{kj} \right. \\ &\quad \left. \times \mathcal{F} \left(\frac{3}{\alpha_r}, d_{jI_1}^{\mathcal{G}_2}, d_{jI_1}^{\mathcal{G}_1} \right) - \mathcal{F} \left(\frac{4}{\alpha_r}, d_{jI_1}^{\max}, d_{jI_1}^{\mathcal{G}_2} \right) + 2d_{kj} \mathcal{F} \left(\frac{3}{\alpha_r}, d_{jI_1}^{\max}, d_{jI_1}^{\mathcal{G}_2} \right) + (D_{\max}^2 - d_{kj}^2) \mathcal{F} \left(\frac{2}{\alpha_r}, d_{jI_1}^{\max}, d_{jI_1}^{\mathcal{G}_2} \right) \right\} \quad (66) \end{aligned}$$

$$\begin{aligned} f_2(s, d_{kj}) &= \mathcal{F} \left(\frac{4}{\alpha_r}, d_{jI_1}^{\mathcal{G}_1}, d_{jI_1}^{\min} \right) + (d_{kj}^2 - D_{\min}^2) \mathcal{F} \left(\frac{2}{\alpha_r}, d_{jI_1}^{\mathcal{G}_1}, d_{jI_1}^{\min} \right) + (D_{\max}^2 - d_{kj}^2) \mathcal{F} \left(\frac{2}{\alpha_r}, d_{jI_1}^{\max}, d_{jI_1}^{\mathcal{G}_2} \right) \\ &\quad + 2d_{kj} \mathcal{F} \left(\frac{3}{\alpha_r}, d_{jI_1}^{\mathcal{G}_1}, d_{jI_1}^{\min} \right) + 4d_{kj} \mathcal{F} \left(\frac{3}{\alpha_r}, d_{jI_1}^{\mathcal{G}_2}, d_{jI_1}^{\mathcal{G}_1} \right) - \mathcal{F} \left(\frac{4}{\alpha_r}, d_{jI_1}^{\max}, d_{jI_1}^{\mathcal{G}_2} \right) + 2d_{kj} \mathcal{F} \left(\frac{3}{\alpha_r}, d_{jI_1}^{\max}, d_{jI_1}^{\mathcal{G}_2} \right) \quad (68) \end{aligned}$$

When $l > 0$, employing the Faà di Bruno's formula, $\Delta^{(l)}(s)$ can be obtained as

$$\begin{aligned} \Delta^{(l)}(s, a, b) &= \sum_{q=1}^l \frac{(m+a)(m)_q}{m+a+q} \\ &\quad \times {}_2F_1\left(m+q, m+a+q; m+a+q+1; -\frac{mb^{\frac{\alpha_r}{2}}}{\Omega s}\right) \\ &\quad \times B_{l,q}\left(f_3^{(1)}(s, b), \dots, f_3^{(l-q+1)}(s, b)\right), \end{aligned} \quad (70)$$

where $f_3(s, b) = -\frac{mb^{\frac{\alpha_r}{2}}}{\Omega} s^{-1}$, and $f_3^{(q)}(s, b) = (-1)^{q+1} q! \frac{mb^{\frac{\alpha_r}{2}}}{\Omega} s^{-1-q}$.

Furthermore, the l th derivative of $\mathcal{F}(a, b, c)$ can be achieved as

$$\mathcal{F}^{(l)}(a, b, c) = \frac{2}{(m+a)\alpha_r} \left[b^{\frac{(m+a)\alpha_r}{2}} \Delta^{(l)}(s, a, b) - c^{\frac{(m+a)\alpha_r}{2}} \Delta^{(l)}(s, a, c) \right]. \quad (71)$$

Combining (68), (70), and (71), we can obtain the l th derivative of $f_2(s)$, $f_2^{(l)}(s)$. Then, (41) can be achieved by substituting (69) and $f_2^{(l)}(s)$ in (67).

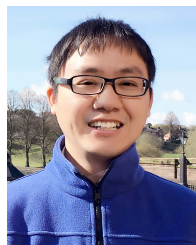
REFERENCES

- [1] G. Pan, J. Ye, Y. Zhang, and M.-S. Alouini, "Performance analysis and optimization of cooperative satellite-aerial-terrestrial systems," *IEEE Trans. Wireless Commun.*, vol. 19, no. 10, pp. 6693–6707, Oct. 2020.
- [2] E. Zedini, A. Kammoun, and M.-S. Alouini, "Performance of multibeam very high throughput satellite systems based on FSO feeder links with HPA nonlinearity," *IEEE Trans. Wireless Commun.*, vol. 19, no. 9, pp. 5908–5923, Sep. 2020.
- [3] G. Pan, J. Ye, Y. Tian, and M.-S. Alouini, "On HARQ schemes in satellite-terrestrial transmissions," *IEEE Trans. Wireless Commun.*, vol. 19, no. 12, pp. 7998–8010, Dec. 2020.
- [4] Y. Kawamoto, T. Kamei, M. Takahashi, N. Kato, A. Miura, and M. Toyoshima, "Flexible resource allocation with inter-beam interference in satellite communication systems with a digital channelizer," *IEEE Trans. Wireless Commun.*, vol. 19, no. 5, pp. 2934–2945, May 2020.
- [5] Z. Lin, M. Lin, T. de Cola, J.-B. Wang, W.-P. Zhu, and J. Cheng, "Supporting IoT with rate-splitting multiple access in satellite and aerial-integrated networks," *IEEE Internet Things J.*, vol. 8, no. 14, pp. 11123–11134, Jul. 2021.
- [6] D. Christopoulos, S. Chatzinotas, and B. Ottersten, "Multicast multi-group precoding and user scheduling for frame-based satellite communications," *IEEE Trans. Wireless Commun.*, vol. 14, no. 9, pp. 4695–4707, Sep. 2015.
- [7] Y. Zhang, J. Ye, G. Pan, and M.-S. Alouini, "Secrecy outage analysis for satellite-terrestrial downlink transmissions," *IEEE Wireless Commun. Lett.*, vol. 9, no. 10, pp. 1643–1647, Oct. 2020.
- [8] E. Illi, F. El Bouanani, F. Ayoub, and M.-S. Alouini, "A PHY layer security analysis of a hybrid high throughput satellite with an optical feeder link," *IEEE Open J. Commun. Soc.*, vol. 1, pp. 713–731, 2020.
- [9] Z. Lin, M. Lin, B. Champagne, W.-P. Zhu, and N. Al-Dhahir, "Secure beamforming for cognitive satellite terrestrial networks with unknown eavesdroppers," *IEEE Syst. J.*, vol. 15, no. 2, pp. 2186–2189, Jun. 2021.
- [10] Z. Lin, M. Lin, B. Champagne, W.-P. Zhu, and N. Al-Dhahir, "Secrecy-energy efficient hybrid beamforming for satellite-terrestrial integrated networks," *IEEE Trans. Commun.*, vol. 69, no. 9, pp. 6345–6360, Sep. 2021.
- [11] Z. Lin, M. Lin, B. Champagne, W.-P. Zhu, and N. Al-Dhahir, "Secure and energy efficient transmission for RSMA-based cognitive satellite-terrestrial networks," *IEEE Wireless Commun. Lett.*, vol. 10, no. 2, pp. 251–255, Feb. 2021.
- [12] M. Zolanvari, R. Jain, and T. Salman, "Potential data link candidates for civilian unmanned aircraft systems: A survey," *IEEE Commun. Surveys Tuts.*, vol. 22, no. 1, pp. 292–319, 1st Quart. 2020.
- [13] Y. Cai, Z. Wei, R. Li, D. W. K. Ng, and J. Yuan, "Joint trajectory and resource allocation design for energy-efficient secure UAV communication systems," *IEEE Trans. Commun.*, vol. 68, no. 7, pp. 4536–4553, Jul. 2020.
- [14] H. Lei *et al.*, "Safeguarding UAV IoT communication systems against randomly located eavesdroppers," *IEEE Internet Things J.*, vol. 7, no. 2, pp. 1230–1244, Feb. 2020.
- [15] A. V. Savkin, H. Huang, and W. Ni, "Securing UAV communication in the presence of stationary or mobile eavesdroppers via online 3D trajectory planning," *IEEE Wireless Commun. Lett.*, vol. 9, no. 8, pp. 1211–1215, Aug. 2020.
- [16] G. Pan, H. Lei, J. An, S. Zhang, and M.-S. Alouini, "On the secrecy of UAV systems with linear trajectory," *IEEE Trans. Wireless Commun.*, vol. 19, no. 10, pp. 6277–6288, Oct. 2020.
- [17] X. Li *et al.*, "A unified framework for HS-UAV NOMA networks: Performance analysis and location optimization," *IEEE Access*, vol. 8, pp. 13329–13340, 2020.
- [18] P. K. Sharma, D. Deepthi, and D. I. Kim, "Outage probability of 3-D mobile UAV relaying for hybrid satellite-terrestrial networks," *IEEE Commun. Lett.*, vol. 24, no. 2, pp. 418–422, Feb. 2020.
- [19] Q. Huang, M. Lin, J. Wang, T. A. Tsiftsis, and J. Wang, "Energy efficient beamforming schemes for satellite-aerial-terrestrial networks," *IEEE Trans. Commun.*, vol. 68, no. 6, pp. 3863–3875, Jun. 2020.
- [20] H. Kong, M. Lin, W.-P. Zhu, H. Amindavar, and M.-S. Alouini, "Multi-user scheduling for asymmetric FSO/RF links in satellite-UAV-terrestrial networks," *IEEE Wireless Commun. Lett.*, vol. 9, no. 8, pp. 1235–1239, Aug. 2020.
- [21] H. Dai, H. Bian, C. Li, and B. Wang, "UAV-aided wireless communication design with energy constraint in space-air-ground integrated green IoT networks," *IEEE Access*, vol. 8, pp. 86251–86261, 2020.
- [22] P. Zhou, X. Fang, Y. Fang, R. He, Y. Long, and G. Huang, "Beam management and self-healing for mmWave UAV mesh networks," *IEEE Trans. Veh. Technol.*, vol. 68, no. 2, pp. 1718–1732, Feb. 2019.
- [23] N. Cheng *et al.*, "Space/aerial-assisted computing offloading for IoT applications: A learning-based approach," *IEEE J. Sel. Areas Commun.*, vol. 37, no. 5, pp. 1117–1129, May 2019.
- [24] C. Liu, W. Feng, Y. Chen, C.-X. Wang, and N. Ge, "Cell-free satellite-UAV networks for 6G wide-area Internet of Things," *IEEE J. Sel. Areas Commun.*, vol. 39, no. 4, pp. 1116–1131, Apr. 2021.
- [25] Y. Zeng, Q. Wu, and R. Zhang, "Accessing from the sky: A tutorial on UAV communications for 5G and beyond," *Proc. IEEE*, vol. 107, no. 12, pp. 2327–2375, Dec. 2019.
- [26] M. Haenggi, *Stochastic Geometry for Wireless Networks*. Cambridge, U.K.: Cambridge Univ. Press, 2012.
- [27] A. M. Hunter, J. G. Andrews, and S. Weber, "Transmission capacity of ad hoc networks with spatial diversity," *IEEE Trans. Wireless Commun.*, vol. 7, no. 12, pp. 5058–5071, Dec. 2008.
- [28] H. He, J. Xue, T. Ratnarajah, F. A. Khan, and C. B. Papadias, "Modeling and analysis of cloud radio access networks using Matérn hard-core point processes," *IEEE Trans. Wireless Commun.*, vol. 15, no. 6, pp. 4074–4087, Jun. 2016.
- [29] A. Omri and M. O. Hasna, "A distance-based mode selection scheme for D2D-enabled networks with mobility," *IEEE Trans. Wireless Commun.*, vol. 17, no. 7, pp. 4326–4340, Jul. 2018.
- [30] S. Bachtobji, A. Omri, R. Bouallegue, and K. Raouf, "Modelling and performance analysis of mmWaves and radio-frequency based 3D heterogeneous networks," *IET Commun.*, vol. 12, no. 3, pp. 290–296, Feb. 2018.
- [31] A. Omri and M. O. Hasna, "Modeling and performance analysis of D2D communications with interference management in 3-D HetNets," in *Proc. IEEE Global Commun. Conf. (GLOBECOM)*, Dec. 2016, pp. 1–7.
- [32] T. S. Rappaport, *Wireless Communications: Principles and Practice*. Englewood Cliffs, NJ, USA: Prentice-Hall, 1996.
- [33] Y. Li, N. I. Miridakis, T. A. Tsiftsis, G. Yang, and M. Xia, "Air-to-air communications beyond 5G: A novel 3D CoMP transmission scheme," *IEEE Trans. Wireless Commun.*, vol. 19, no. 11, pp. 7324–7338, Nov. 2020.
- [34] M. Grover, P. Singh, P. Kaur, and C. Madhu, "Multibeam WDM-FSO system: An optimum solution for clear and hazy weather conditions," *Wireless Pers. Commun.*, vol. 97, no. 4, pp. 5783–5795, Dec. 2017.
- [35] (2021). *DoD Space Agency to Create Marketplace for Commercial Satellite Data*. Accessed: Jun. 22, 2021. [Online]. Available: <https://breakingdefense.com/2021/06/sda-demos-spotlight-tech-hurdles-to-jadc2-backbone/>
- [36] S. N. Chiu, D. Stoyan, W. S. Kendall, and J. Mecke, *Stochastic Geometry and Its Applications*. Hoboken, NJ, USA: Wiley, 2013.

- [37] S. Karp, R. M. Gagliardi, S. E. Moran, and L. B. Stotts, *Optical Channels: Fibers, Clouds, Water and the Atmosphere*. New York, NY, USA: Plenum, 1988.
- [38] A. Goldsmith, *Wireless Communications*. Cambridge, U.K.: Cambridge Univ. Press, 2005.
- [39] G. Pan, H. Lei, Z. Ding, and Q. Ni, "On 3-D hybrid VLC-RF systems with light energy harvesting and OMA scheme over RF links," in *Proc. IEEE Global Commun. Conf. (GLOBECOM)*, Dec. 2017, pp. 1–6.
- [40] I. S. Gradshteyn and I. M. Ryzhik, *Table of Integrals, Series, and Products*. New York, NY, USA: Academic, 2014.
- [41] I. S. Ansari, F. Yilmaz, and M.-S. Alouini, "Performance analysis of FSO links over unified gamma-gamma turbulence channels," in *Proc. IEEE 81st Veh. Technol. Conf. (VTC Spring)*, May 2015, pp. 1–5.
- [42] X. Lei, L. Fan, D. S. Michalopoulos, P. Fan, and R. Q. Hu, "Outage probability of TDBC protocol in multiuser two-way relay systems with Nakagami- m fading," *IEEE Commun. Lett.*, vol. 17, no. 3, pp. 487–490, Mar. 2013.
- [43] X. Liu, M. Lin, W.-P. Zhu, J.-Y. Wang, and P. K. Upadhyay, "Outage performance for mixed FSO-RF transmission in satellite-aerial-terrestrial networks," *IEEE Photon. Technol. Lett.*, vol. 32, no. 21, pp. 1349–1352, Nov. 1, 2020.
- [44] Y. Ai, A. Mathur, M. Cheffena, M. R. Bhatnagar, and H. Lei, "Physical layer security of hybrid satellite-FSO cooperative systems," *IEEE Photon. J.*, vol. 11, no. 1, pp. 1–14, Feb. 2019.
- [45] M. K. Simon and M.-S. Alouini, *Digital Communication Over Fading Channels*, 2nd ed. New York, NY, USA: Wiley, 2005.



Yu Tian received the B.Sc. degree in communication engineering from the Harbin Institute of Technology in 2013 and the M.Sc. degree from the King Abdullah University of Science and Technology (KAUST), Saudi Arabia, in 2019, where he is currently pursuing the Ph.D. degree. His current research interests include deep learning and performance analysis of wireless communication systems.



Gaofeng Pan (Senior Member, IEEE) received the B.Sc. degree in communication engineering from Zhengzhou University, Zhengzhou, China, in 2005, and the Ph.D. degree in communication and information systems from Southwest Jiaotong University, Chengdu, China, in 2011. He is currently with the School of Cyberspace Science and Technology, Beijing Institute of Technology, China, as a Professor. His research interest spans special topics in communications theory, signal processing, and protocol design.



Mustafa A. Kishk (Member, IEEE) received the B.Sc. and M.Sc. degrees from Cairo University in 2013 and 2015, respectively, and the Ph.D. degree from Virginia Tech in 2018. He is currently a Post-Doctoral Research Fellow with the CTL at KAUST. His current research interests include stochastic geometry, energy harvesting wireless networks, UAV-enabled communication systems, and satellite communications.



Mohamed-Slim Alouini (Fellow, IEEE) was born in Tunis, Tunisia. He received the Ph.D. degree in electrical engineering from the California Institute of Technology (Caltech), Pasadena, CA, USA, in 1998. He worked as a Faculty Member with the University of Minnesota, Minneapolis, MN, USA, then with Texas A&M University, Qatar, Education City, Doha, Qatar, before joining the King Abdullah University of Science and Technology (KAUST), Thuwal, Makkah, Saudi Arabia, as a Professor in electrical engineering, in 2009. His current research interests include modeling, design, and performance analysis of wireless communication systems.